

Chapter 6

Systematic Uncertainty Descriptions and Estimates

In this chapter the systematic uncertainties related to the measurement of $P_\mu\xi$ are estimated. The overall systematic uncertainty is estimated as the quadrature sum of individual sensitivity measurements S_i divided by a scale factor. The scale factor comes from the change R_i introduced to measure the sensitivity to the systematic effect over the RMS change (σ_i) in the systematic effect in data. The total systematic uncertainty is thus equal to:

$$\epsilon_{sys}^{tot} = \sqrt{\sum_i \frac{\sigma_i^2}{R_i^2} S_i^2} \quad (6.1)$$

Systematic uncertainties are divided into set dependent uncertainties, and set independent uncertainties. The set dependent uncertainties are added in quadrature with the individual set statistical uncertainties in calculating the weighted average offset of $P_\mu\xi$ from the black-box value. The detailed listing of the systematic uncertainties is given in Table 6.1. The uncertainties labelled with (ave) were considered to be set dependent. The total systematic uncertainty of $\pm 3.8 \times 10^{-3}$ is obtained for this measurement of $P_\mu\xi$. The estimate for fringe field depolarization systematic uncertainty dominates the measurement uncertainty.

In many cases the error in the sensitivity measurement was larger than the sensitivity itself, such that a meaningful sensitivity was not measured. For those cases, the random value that we determined for the sensitivity was used in the same way as the other measured sensitivities. It is expected that on average this method should give the best statistical estimate of the systematic uncertainty [51].

It should be noted that every effort was made to try to avoid double counting of the systematic uncertainty by separating effects into orthogonal uncertainties. Inevitably there will be some overlap that cannot be avoided.

The following sections discuss in detail the systematic uncertainties categorized as:

1. muon beam characteristics and polarization
2. chamber response
3. momentum calibration
4. positron interactions
5. spectrometer alignment

For the systematic uncertainties that change from set to set, the method of obtaining the overall systematic uncertainty, and the set to set variation are discussed in the relevant sections. A tabulation of the set-to-set uncertainties is in the final section of this Chapter.

Category	Sensitivity		Scale R_i/σ_i	Systematic Uncertainty
	S_i Value	S_i Error		
Muon beam and polarization				± 3.69
Fringe field (ave)				3.40
Depolarization in stopping material (ave)				1.40
Depolarization in production target				0.21
Background muon contamination (ave)				0.18
Beam intensity (ave)	-3.0	1.7	16.3	0.18
Chamber response				± 0.98
t0 variations (ave)	8.9	0.9	10	0.89
Foil bulges (ave)	2.2	1.4	10	0.22
Cell asymmetry	-0.2	1.4	1	0.22
Up-down efficiency	1.9	0.9	10	0.19
Density (ave)	2.4	1.4	14.3	0.17
Dead zone	0.2	1.4	12	0.01
Spectrometer alignment				± 0.31
z	2.2	1.0	10	0.22
Rotations	8.5	0.8	39	0.22
B field to axis	1.2	1.4	40	0.03
Translations	0.1	0.8	28	0.00
Positron interactions				± 0.30
Hard and intermediate interactions (ave)				0.29
Multiple scattering	-3.2	1.4	40	0.08
Outside material	1.2	2.0	60	0.02
Energy Loss	0.6	0.2	100	0.01
Momentum calibration				± 0.19
End point fits				0.16
B uniformity	-0.9	0.4	10	0.09
Theoretical radiative corrections				± 0.10
Total In Quadrature				± 3.8

Table 6.1: Table of Systematic Uncertainties in $P_{\mu\xi}$ in units of $\times 10^{-3}$. The top line of each category shows the quadrature sum of the systematic uncertainty for that category. The average systematic uncertainties are given for the set dependent systematic uncertainties denoted with (ave). In the case that a sensitivity was measured using correlated analyses, the error in the sensitivity was multiplied by the square root of the fit $\chi^2/NDOF$.

6.1 Systematic Uncertainty Due to Muon Beam Characteristics and Polarization

In bringing the muon beam to a stop at the center of the *TWIST* spectrometer, the muons can be depolarized by the combination of multiple scattering and interaction with the fringe field of the spectrometer, and by spin relaxation or other interactions in the vicinity of the muon stopping target.

This section will discuss the systematic uncertainties due to:

1. muon depolarization in the production target
2. muon depolarization in the beamline window valve
3. muon beam transfer through the solenoid fringe field
4. muon depolarization at the stopping location
5. beam contamination with background muons
6. beam intensity and accidental particles
7. proton beam stability

Note that the muon depolarization in the beamline window valve is estimated in this section, but not included in the overall table of systematic uncertainties because its effect is very small.

6.1.1 Depolarization in the Muon Production Target

This section estimates the systematic uncertainty due to depolarization in the production target. The effect is estimated to be negligible compared to the statistical uncertainty obtained with the data taken in 2003 to try to measure this effect. The 2003 data are not being used since the uncertainty in $P_\mu\xi$ from the data-to-data fit is too large to be useful.

The M13 beamline has $\frac{\delta p}{p}$ of 1% (FWHM) meaning that we have a range of roughly 29.4 to 29.8 MeV/c for our nominal surface muon beam momentum of 29.6 MeV/c. To obtain a conservative estimate of the depolarization in the production target we include a little extra for tails of the non-Gaussian distribution. This is a range of 0.4 MeV/c.

$\frac{dp}{dx}$ for this momentum is about 55 MeV/c/(g/cm²) for our graphite production target described in Section ???. Thus the difference in thickness corresponding to 0.4 MeV/c, which is a good estimate of the effective maximum depth from which our muons are born, is 0.007 g/cm². Using a density of 2.26 g/cm³ the production depth is 0.003 cm of graphite.

Using the multiple scattering formula in Equation 6.2, the multiple scattering angle in graphite can be estimated. X_0 is 42.7 g/cm², so $x/X_0 = 0.007/42.7 = 0.00016$, which is well below the quoted range of validity for the multiple scattering formula. However, for muons moving with velocity $\beta = 0.265$ we obtain $\theta_{space}^{RMS} = 0.0206$ rad.

$$\theta_{space}^{RMS} = \sqrt{2} \frac{13.6 \text{ MeV}}{\beta c p} z \sqrt{x/X_0} [1 + 0.038 \ln x/X_0] \quad (6.2)$$

An estimate of the depolarization in the small angle approximation is $(\theta_{space}^{RMS})^2/2$. This works out to a contribution of 0.21×10^{-3} .

6.1.2 Depolarization in the Beamline Window Valve

An 0.0003 cm thick polyester foil was inserted in the beamline to reduce the amount of beam gas making it to the end of the beamline. The density of polyester is about half the density of graphite, so using the arguments of the previous section we find $\frac{dp}{dx}$ is about 28 MeV/c/(g/cm²), meaning the muons lose about 8 keV going through the foil. Using the PDG multiple scattering formula with $X_0 = 40.0$ g/cm² the value of x/X_0 is 0.000010. For muons with velocity $\beta = 0.265$ we obtain $\theta_0 = 0.0031$. Using the small angle approximation for depolarization this works out to be a contribution to the systematic uncertainty of 5×10^{-6} .

6.1.3 Fringe Field Depolarization (FFD)

This subsection describes the systematic uncertainty in $P_\mu\xi$ due to the apparent depolarization of muons passing through the fringe field of the TWIST solenoid. The systematic uncertainty is estimated from a combination of: beam position and angle uncertainty, uncertainty in the magnetic field shape in the fringe field region, and the deconvolution of the beam angle distribution widths measured with the TEC.

The final systematic uncertainty in $P_\mu\xi$ due to fringe field depolarization will be described in detail in the following sub-subsections on:

1. beam position and angle uncertainty ($\pm 3.3 \times 10^{-3}$)
2. deconvolution of the TEC beam angles ($\pm 0.7 \times 10^{-3}$)
3. magnetic fringe field shape ($\pm 0.3 \times 10^{-3}$)
4. beam size reproduction ($\pm 0.35 \times 10^{-3}$)

The total systematic uncertainty in $P_\mu\xi$ due to fringe field depolarization is $\pm 3.40 \times 10^{-3}$. A conservative estimate has been made since a data validation of our simulation polarization estimates was not obtained.

FFD: Beam Position and Angle Uncertainty

In this section the sensitivity and systematic uncertainty in $P_\mu\xi$ due to beam position and angle is estimated. The uncertainty in the beam measurement is estimated by comparing the range of predicted polarizations in the simulation for the different beam tunes used in data taking.

To confirm the systematic uncertainty chosen, another estimate based on a best guess at the uncertainty in the TEC to yoke alignment is reviewed. In Section ??, the uncertainty in the beam position was estimated to be ± 2 mm in any direction, and the uncertainty in the beam angle was estimated to be ± 5 mrad.

Another measure of the uncertainty in the beam measurement comes from a comparison of the muon beam as seen inside the detector in both simulation and Data. The u and v

coordinates of the muon at the last two PCs before the muons stopping target are available from the output of the analysis of both data and simulation. From distributions of the muon u and v coordinates, the average ($\langle u \rangle$ and $\langle v \rangle$) and RMS (RMS u , RMS v) values can be compared between data and simulation. The comparison of these muon beam parameters is shown in Fig. 6.1. The mean positions in the data and simulation track each other fairly well, with differences in position of < 1.5 mm in $\langle u \rangle$ and < 1 mm in $\langle v \rangle$. The RMS size of the beam is about 1.5 mm larger in simulation than in data. The uncertainty due to the poor reproduction of the beam size is discussed in Section 6.1.3. Comparing the $\langle u \rangle$ and $\langle v \rangle$ between Set 30 and Set 35 shows that the beam moves about 5 mm inside the detector when B2 is changed by 5 G. This is a consequence of the focusing effect of the solenoid field, since the beam at the TEC moves by about 10 mm when B2 is changed by 5 G.

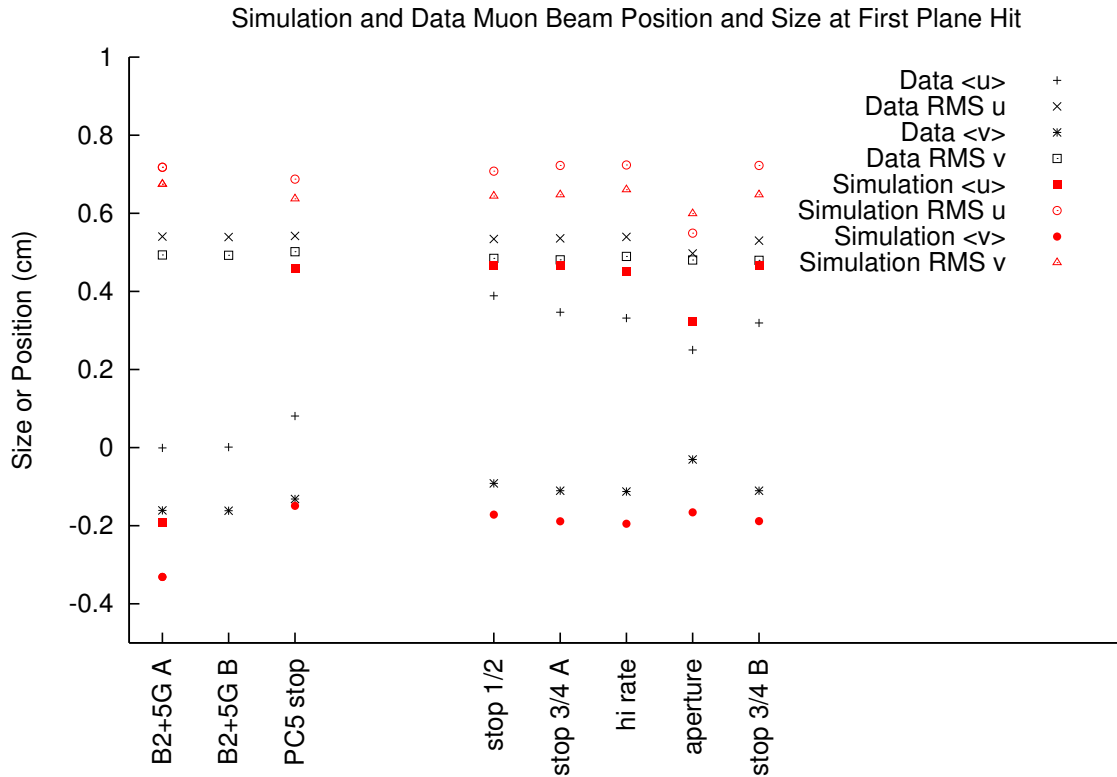


Figure 6.1: The match between the beam position mean and RMS values at the stopping target for each of the data sets considered. The units on the vertical scale are cm.

To estimate the sensitivity to fringe field depolarization, the beam input into simulation was scanned over the range ± 2 cm and ± 20 mrad in both x and y . The result of this scan shows that the polarization versus beam shift can be approximated by a quadratic polynomial. The scan results for the nominal beam are shown in Figure 6.2.

The quadratic function given in Equation 6.5, where the x , y , dx and dy represent the

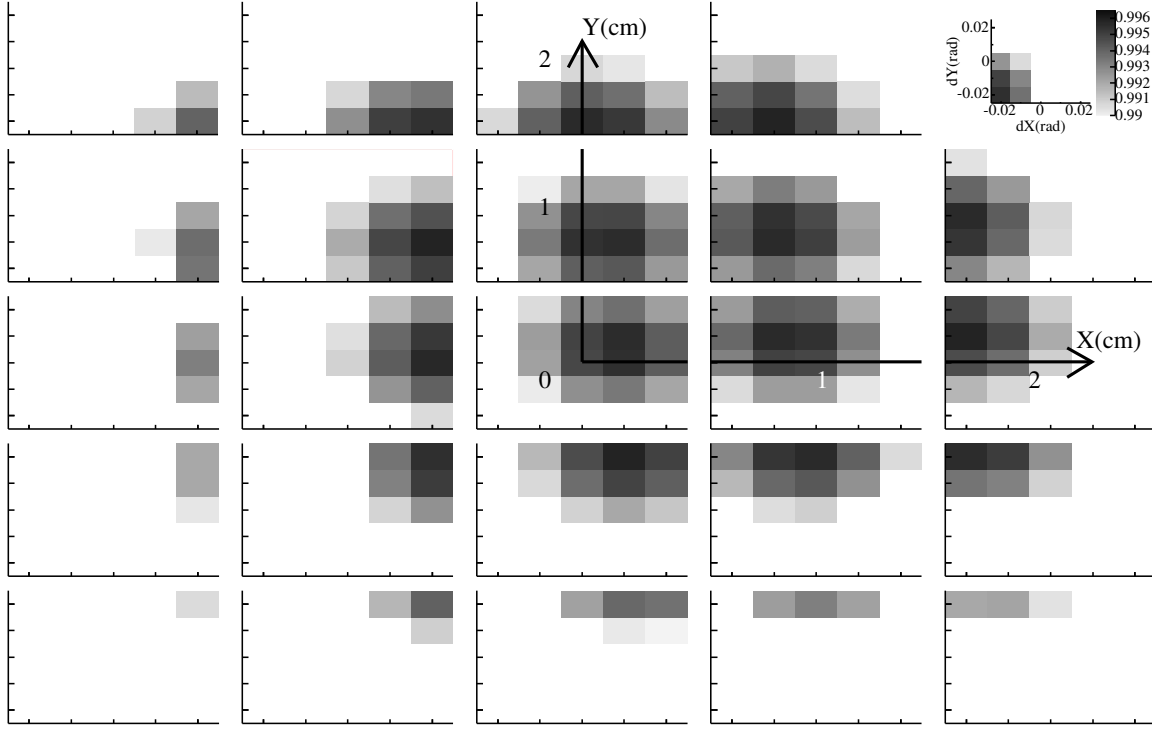


Figure 6.2: Fringe Field Sensitivity simulation Scan showing the mean spin along the z axis for muons that stop in the target, where red is the highest polarization of 0.9965, and blue is the lowest polarization of 0.99. An unshaded or white square is lower polarization than 0.99. Each of the 25 plots shown here is a polarization for each shift in dy versus dx from +20 mrad to -20 mrad. The middle plot is for an unshifted beam, plots on the first row are for the beam shifted up by 2 cm at the TEC, the second row shifted up by 1 cm, and so on filling the matrix of beam shifts in x and y from +2 cm to -2 cm.

shifts in the positions and angles, was used to fit the data.

$$P_{\mu}(x, y, dx, dy) = P_{max} + A((dx - x_0)^2 + (dy - y_0)^2) \quad (6.3)$$

The fit constants P_{max} and A were roughly independent of the shift in x and y , while the fit constants x_0 and y_0 were found to be functions of x and y .

Fits to x_0 versus x and y , and y_0 versus x and y can be done to find the constants in the linear equations:

$$x_0 = x_{00} + x_{0x} x \quad (6.4)$$

$$x_0 = x_{00} + x_{0y} y$$

$$y_0 = y_{00} + y_{0x} x$$

$$y_0 = y_{00} + y_{0y} y$$

The overall four dimensional polynomial can then be written:

$$P_\mu(x, y, dx, dy) = P_{max} + A((dx - x_{00} - x_{0x} x - x_{0y} y)^2 + (dy - y_{00} - y_{0x} x - y_{0y} y)^2) \quad (6.5)$$

The constants in this polynomial for the standard beam tune are summarized in Table 6.2. Residuals from the polynomial fit show that the using the polynomial as an estimate of the polarization is only good to about 1.5×10^{-3} .

Parameter	Nominal Tune	Aperture	+5 gauss	High Rate	Units
P_{max}	0.9958	0.9976	0.9950	0.9954	
A	-9.796	-10.536	-8.548	-9.831	rad^{-2}
x_{00}	0.0075	0.0067	0.0106	0.0075	rad
x_{0x}	-0.0129	-0.0121	-0.0142	-0.0133	rad/cm
x_{0y}	-0.0032	-0.0021	-0.0041	-0.0030	rad/cm
y_{00}	0.0058	0.0038	0.0167	0.0057	rad
y_{0x}	0.0024	0.0002	0.0020	0.0025	rad/cm
y_{0y}	-0.0137	-0.0122	-0.0149	-0.0138	rad/cm

Table 6.2: Beam polarization polynomial parameters from fit to simulation scans of the different beam tunes.

The four dimensional polynomial can be used to plot the sensitivity of the polarization to the estimated shifts in the beam. For an uncertainty in the beam position of ± 2 mm, and uncertainty in the beam angle of ± 5 mrad, the systematic uncertainty in $P_\mu \xi$ is ± 0.0015 for the nominal beam tune. The systematic uncertainty due to fringe field depolarization for the different beam tunes used in 2004 is summarized in Table 6.4.

A second input to the systematic uncertainty due to the beam comes from TEC runs of the same beam settings taken at different times during the 2004 data taking. Values of the average beam positions and angles from TEC measurements of the beam are summarized in Table 6.1.3. Clearly there were issues with either the alignment or efficiency of the TEC between these two measurements. The relative changes in angle and position between the nominal and B2+5 G are roughly the same, but the absolute numbers for the average beam angle are quite different. To estimate the effect of this change in the beam measurement on the polarization estimate, the mean positions and angles were plugged into Equation 6.5 that is described later in this section. The larger difference in polarization of 3.3×10^{-3} between the two measurements of the beam at 949 G is an estimate of the systematic uncertainty in the value of P_μ .

In Section 7.1.1 we note that the values of $P_\mu \xi$ in the data are consistent, while the simulation predicts a difference in polarization of 6.1×10^{-3} . Since the confirmation of the simulation was not obtained yet, and there is some ambiguity in the absolute polarization based on the beam tunes available, half the difference observed in simulation, 3.1×10^{-3} , is an estimate of the systematic uncertainty in $P_\mu \xi$ that is consistent with the 3.3×10^{-3} between the two measurements of the beam at 949 G. The systematic uncertainty in $P_\mu \xi$ is thus quoted as 3.3×10^{-3} due to the ambiguity in absolute polarization predicted by the TEC beam tunes.

B2 (gauss)	$\langle x \rangle$ (cm)	$\langle dx \rangle$ (mrad)	$\langle y \rangle$ (cm)	$\langle dy \rangle$ (mrad)	Polynomial P_μ
949	0.85	-1.1	0.87	-5.0	0.9955
946.5	0.45	-3.4	0.92	1.8	0.9952
944	0.07	-5.9	0.97	7.0	0.9929
941.5	-0.29	-8.3	1.03	10.0	0.9897
949	0.94	-1.5	0.64	-19.2	0.9922
944	0.06	-6.7	0.73	-11.2	0.9941

Table 6.3: Average beam positions and angles from TEC measurements of the beam during a B2 scan. The last two rows show the TEC measurements for the characterization runs used in the simulation.

Beam Tune	Nominal	Aperture	+5 gauss	High Rate
Systematic Uncertainty	± 0.0015	± 0.0015	± 0.0035	± 0.0018

Table 6.4: Systematic uncertainty in $P_\mu \xi$ due to uncertainty in beam position and angle for each of the beam tunes used during 2004 data collection.

FFD: Different Field Maps

This section describes the contribution to the systematic uncertainty in $P_{\mu\xi}$ due to uncertainty in the magnetic field map in the fringe field region. To estimate the systematic uncertainty due to the quality of the magnetic field maps, several different field maps are considered. The field maps considered are:

1. The nominal field map generated by Opera as described in Section ??
2. A quarter model field map that included steel from two of the beamline quadrupoles on one of the beamline dipoles that are closest to the solenoid[?]
3. An full model 2.0 T field map that was not fully matched to the measurements of the magnetic field [?]
4. An full model 1.96 T field map from the same Opera model as the map 2 of this list, but with the currents scaled [?]
5. A 1.96 T field map scaled by 0.98 from the nominal field map, but with the fringe field scaled by 0.955 using a method similar to the previous item
6. A 2.04 T field map scaled by 1.02 from the nominal field map, but with the fringe field scaled by 1.045 as in the previous items

The largest difference in polarization as predicted by simulation for a nominal 2004 beam tune using the field maps enumerated above was $< 0.3 \times 10^{-3}$. This value is used as the systematic uncertainty in $P_{\mu\xi}$ due to the quality of the magnetic field map.

FFD: Deconvolution of TEC Multiple Scattering

Multiple Scattering in the different components of the TEC broadens the distribution of angles measured. Simulation was used to estimate Gaussian deconvolution factors needed to reproduce the angular distributions of the beam. The factors obtained were 0.615 for the width of the angle in x, and 0.444 for the width of the angle in y (good to about 10%.) To estimate a systematic uncertainty due to deconvolution of the beam angular distributions measured from the TEC, beam inputs with different deconvolution factors were used. A plot of the simulation predicted polarization versus deconvolution factor is shown in Figure 6.3. The resulting systematic uncertainty due deconvolution of multiple scattering in the measured beam input is 0.5×10^{-3} .

The deconvolution does not account for the non-Gaussian tails that the TEC measurement has. To account for this effect, the difference in polarization, 0.5×10^{-3} , predicted by simulation using the TEC aperture characterization run without the aperture inserted in GEANT versus the same characterization run with the aperture inserted is used. If we add in quadrature the contribution to the systematic uncertainty from deconvolution of the central part of the beam, and from the non-Gaussian tails of the beam, the systematic uncertainty in $P_{\mu\xi}$ due to deconvolution of the TEC beam becomes ± 0.71 .

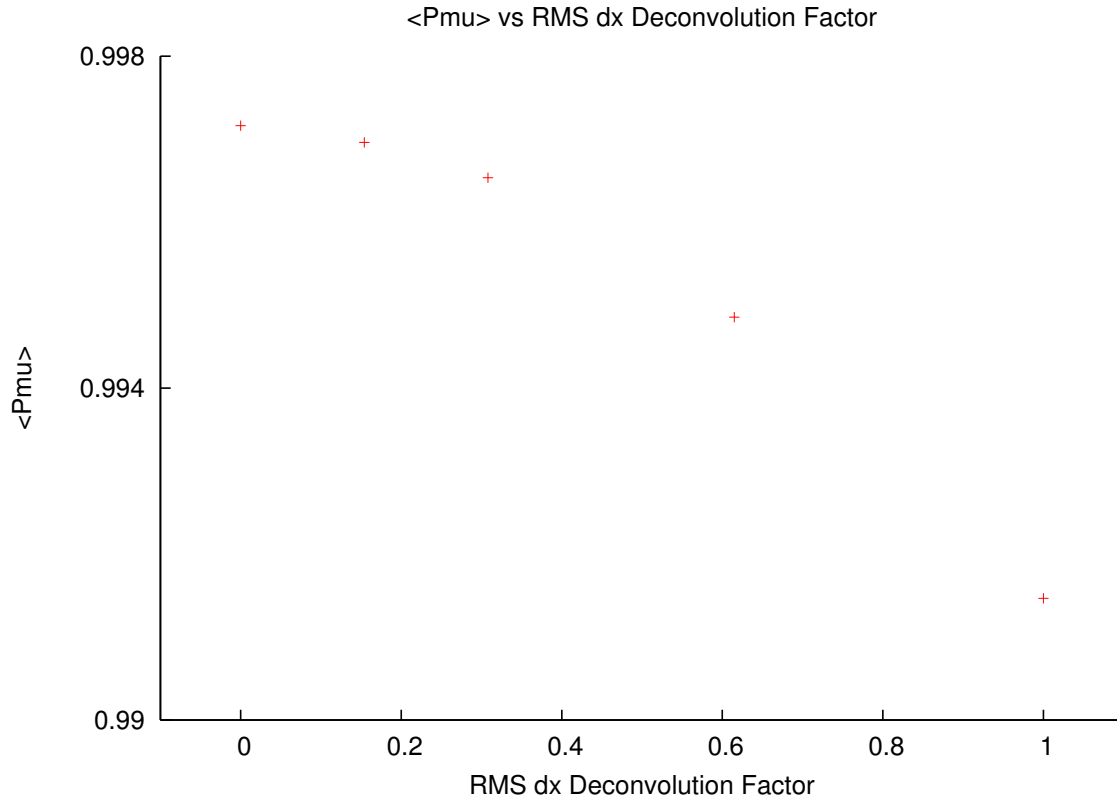


Figure 6.3: Muon polarization versus beam angular width deconvolution factor. Note that the deconvolution factor of the width of the angle in x is plotted here, but that the y deconvolution factor was changed at the same time in the proportion $x/y:0.615/0.444$.

FFD: Muon Beam Size

The simulation muon beam has been observed to be 1.5 mm larger at the stopping target than the muon beam in data. The RMS beam size at the target versus at the TEC for a scan of different starting beam sizes in simulation, and for data sets 35, 37, and 38 are shown in Fig. 6.4. The simulation beam size scan was done starting with the beam input file from set 35 for the angle distributions, but imposing a two-dimensional (2D) Gaussian for the y versus x profile. The means of the profile were the same as the beam in set 35. While a 2D Gaussian does not include the tails of the real beam, or the correlation between x and y of the real beam, the polarization predicted by the beam with a Gaussian width the same as the real beam was witnessed to match at the 10^{-4} level.

A simulation point with zero beam size was simulated using a pencil beam started at $x = y = dx = dy = 0$ at the location of the TEC. It is observed that the pencil beam from the simulation is larger at the stopping target than the real beam in data. To try to understand the source of the large simulation beam size at the stopping target two simulation

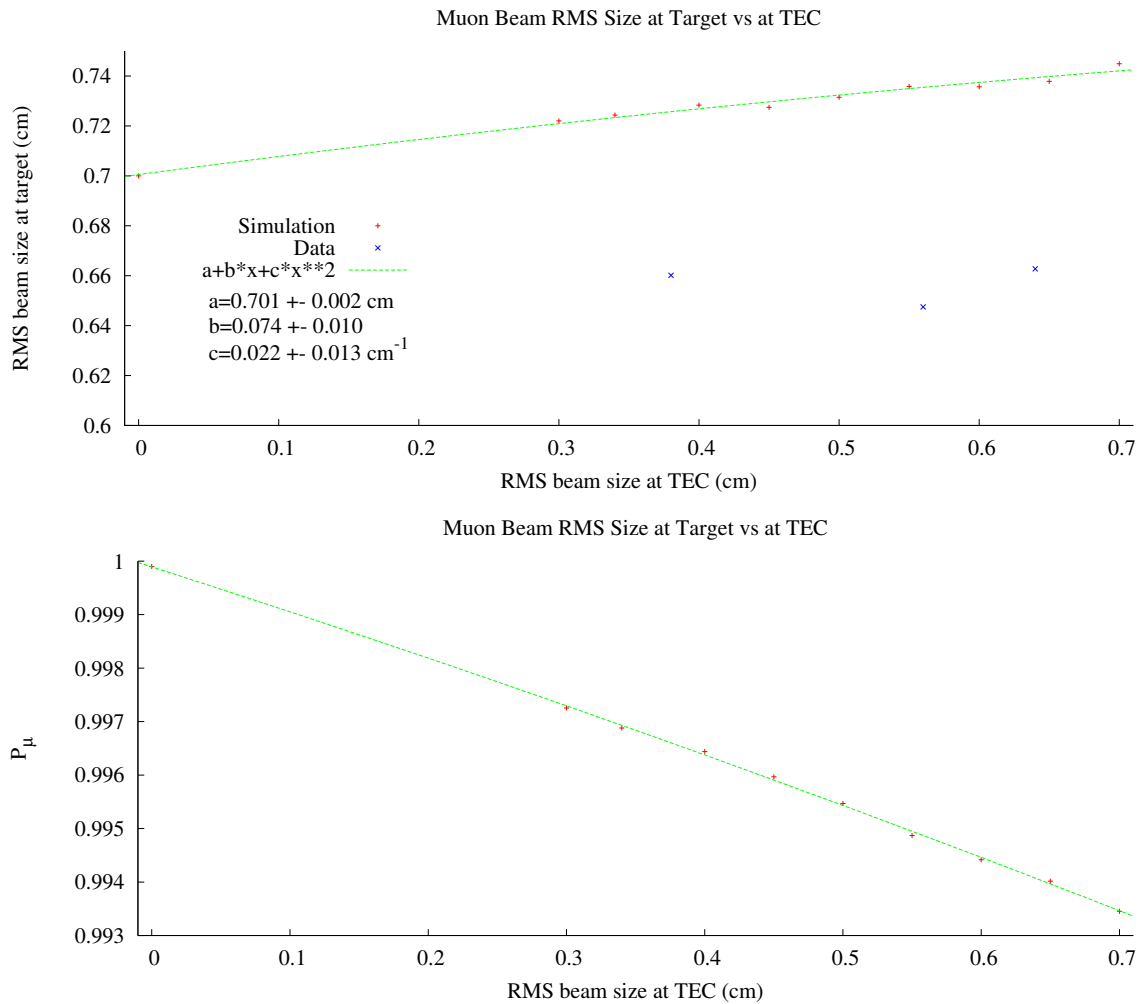


Figure 6.4: The top plot shows the muon beam size at the stopping target versus at the TEC in simulation as the red '+' symbols and in Data as the blue 'x'. The bottom plot shows the muon polarization predicted by the simulation for different muon beam sizes at the TEC.

tests were done. A pencil beam, with all physics processes turned off, was simulated. The result of this simulation was that the muon beam size was zero at the muon stopping target as expected. Then a pencil beam with all physics on, except multiple scattering turned off, was simulated. A muon beam size of 0.045 cm was obtained from this test. The conclusion of these tests is that the muon beam size in simulation is due to the simulation of multiple scattering for muons. The multiple scattering of low energy muons in our simulation is predicting a beam size at the stopping target that is larger than in reality.

The uncertainty in the final polarization estimate due to a discrepancy in the simulation multiple scattering of muons is very small. As a rough estimate of the mean multiple scattering angle with focusing of the solenoid field, consider the beam size of the pencil beam after about one meter of scattering before coming to a stop: $\theta_0 \approx 0.7 \text{ cm} / 100 \text{ cm} \approx 7 \text{ mrad}$. Using the small angle approximation, $1 - |P_\mu| \approx (\theta_0)^2/2$, we obtain a systematic uncertainty in $P_\mu\xi$ of 2×10^{-5} .

To estimate the systematic uncertainty due to the uncertainty in the beam size, the beam size outside the TEC is used since the multiple scattering makes the beam size inside the detector too large in the simulation. A plot of the predicted polarization versus beam size is shown in Fig. 6.4. The nominal RMS beam size is 0.55 cm at the stopping target, or 0.65 cm at the TEC. Since these beam sizes are roughly the same, we take the uncertainty in how well the TEC measures the beam size as the uncertainty in beam size. The resolution of the TEC is about 250 μm , resulting in a systematic uncertainty in $P_\mu\xi$ due to beam size of 0.35×10^{-3} .

6.1.4 Muon Depolarization at the Stopping Location (MDSL)

This section will introduce physics mechanisms that could result in muon depolarization due to interactions in material. The systematic uncertainty due to muon depolarization in gas or Al stopping target is then estimated as the uncertainty due to the extrapolation of a time dependent depolarization to zero decay time. This estimate assumes there is no unobservable depolarization on a time scale < 250 ns.

MDSL: Mechanisms for Muon Depolarization in Materials

Down to about 30 keV the energy loss of muons is mainly due to ionization of atoms along the path of the muon which does not depolarize the muons. Below 30 keV, the thermalization of muons depends strongly on the material. In non-metals, the muons can be captured to form a bound state of a muon and an electron (muonium, written chemically as Mu), which can undergo spin exchange with the electron resulting in depolarization of the muons. In metals there is no Mu formation. Muons in metals will either stop at an interstitial site between metal atoms, or very rarely take the place of an impurity in the metal lattice. The conduction electrons, whose spins should align with the magnetic field of the TWIST solenoid act to screen the muon from Mu formation [19].

At the 99% level, there is no depolarization in a high purity metal target if there is a huge holding field such as we have in TWIST. However at the 99.9% level this is less certain. The Muon creates a quasi-free state in Al where conduction electron concentration is $\simeq 2 \times 10^{23}$ cm^{-3} . The polarized muon state is not stable because the energy difference between the parallel and anti-parallel spin states of a muon in a 2 T magnetic field is $\simeq 10^{-6}$ eV while the thermal energy at $T = 300$ K is $kT \simeq 3 \times 10^{-2}$ eV. Muon spin relaxation can only occur by interaction with the conduction electrons, nuclear moments of the Al, or with paramagnetic impurities in the metal. This section will present an analysis of the possible relaxation time dependence due to these interactions.

Interactions of the muon spin with conductive electrons is called Korringa relaxation [63]. Conduction electrons create a large hyperfine magnetic field at the site of the muon which can be considered as a fluctuating local field with a correlation time $\tau_c \simeq 10^{-13}$ s in Al [64]. This short correlation time results in a relaxation rate that has an exponential form. The Korringa relaxation rate does not depend on the magnetic field. Significant relaxation rates of $\lambda > 0.001 \mu\text{s}^{-1}$ have been measured for muons in Cd, Sn, Pb, As, Sb, and Bi [65]. The authors explained the measured relaxation rates to be due to Korringa relaxation since the λ values increase with temperature as predicted. In our Al target with a longitudinal field $H_L = 2$ T, the muon relaxation rate was measured to be $\lambda = 0.00155 \mu\text{s}^{-1}$. This relaxation rate is most likely to be due to Korringa relaxation (exponential).

Nuclear dipole moments of Al produce magnetic fields, H_d , of few gauss on a muon fixed in a crystal cell. According to many μ^+SR references the dipole-dipole interactions cause muon spin relaxation rates of $\lambda_d = 0.1$ to $0.3 \mu\text{s}^{-1}$ in an orthogonal magnetic field. A longitudinal field, H_L , decreases the amplitude of the relaxation by the factor $(H_d/H_L)^2$ [66]. The reduction of the relaxation rate at $H_L = 2$ T is on the order of $< 10^{-6}$. The above is correct for a muon fixed in a crystal cell. Diffusion of the muon creates a magnetic field

on the muon which varies in both space and time. As a result, the muon relaxation rate decreases and becomes exponential.

Our high purity Al stopping target has the following impurities in ppm: Cu 0.3, Fe 0.3, Mg 1.2, and Si 0.8. Iron is the only paramagnetic impurity that can cause a relaxation. It is unlikely that this can cause much depolarization because we have only one Fe atom for every 3×10^7 atoms of Al. Hence the probability for a muon to reach an Fe atom is very low. If a muon does reach the vicinity of an iron atom, then the magnetic moment from the Fe atom creates a magnetic field $H_e \simeq 1$ kG at a distance of one Al lattice cell period ($\simeq 4 \text{ \AA}$). This magnetic field corresponds to a muon Larmor precession with frequency of $\omega_0 \simeq 10^8 \text{ s}^{-1}$. The interaction causes a very fast muon relaxation if the muon is fixed near the Fe and the Fe electron spin is also fixed. The electron spin of an iron impurity in Al fluctuates with time $\tau_c < 10^{-10} \text{ s}$ [67]. The fluctuations decrease the relaxation rate, and the relaxation dependence becomes exponential when $\omega_0 \cdot \tau_c \ll 1$ [66]. We have $\omega_0 \cdot \tau_c \simeq 10^{-2}$, therefore this unlikely interaction with an iron impurity causes an exponential relaxation. A relaxation rate of $\sigma \simeq 0.02 \mu\text{s}^{-1}$ has been obtained in Al at $T > 100 \text{ K}$ with Fe admixture of 10 ppm by Hartmann *et al.* [68]. Our data also have $\sigma \simeq 0.02 \mu\text{s}^{-1}$ when fitting to a Gaussian depolarization rate. The depolarization rate independence in Al due to the increased iron concentration in the Al of Hartmann is direct evidence that the measured muon relaxation rate is not due to the Fe impurity. The relaxation rate of Hartmann was measured in an orthogonal magnetic field. The rate independence from longitudinal versus orthogonal magnetic field up to $H_L = 2 \text{ T}$ is direct evidence of Korringa relaxation of the muon spin in Al.

High energy muons can create defects in matter. The paramagnetic defects can produce significant magnetic fields on a stopped muon. The defect in the electron configuration recovers in $\sim 10^{-11} \text{ s}$ in metals [69]. The fast recovery can only cause a fast muon relaxation. A muon can also displace atoms in a crystal cell. The displaced atom configuration changes very slowly. The average distance between a stopped muon and the last displaced atom in graphite, for example, is 9000 \AA [70]. The effect of this interaction on the muon relaxation rate is negligible.

In summary the only practical form for muon spin relaxation in our high purity Al target is Exponential; the dominant process being Korringa relaxation by interaction of the muon with conduction electrons.

MDSL: Materials in the Vicinity of the Muon Stopping Target

In the *TWIST* analysis, muons with a hit in PC6 and not in PC7 are considered to have stopped in the stopping target. While this is often the case, we can use our GEANT simulation to study how often the muons stop in other materials near the stopping target (proportional chambers PC5 to PC8.) The proportional chambers consist of: aluminized Mylar foils (or 99.99% purity Al between PC6 and PC7), CF4/i-C4H10 gas, and Gold plated Tungsten wires. A plot from a simulation of where the muon stops versus z coordinate reveals the fraction of muons stopping in different materials. We label the muon stopping fractions as f_j^i , where $i=5,6,7$ labels the selection of last proportional chamber hit by the muon, and $j=\text{Metal(m)}, \text{Other(o)}, \text{Gas(g)}, \text{Plastic(p)}$ labels the material. Figure 6.5 shows the simulated distribution in z of muons stopping in the chambers around the stopping target.

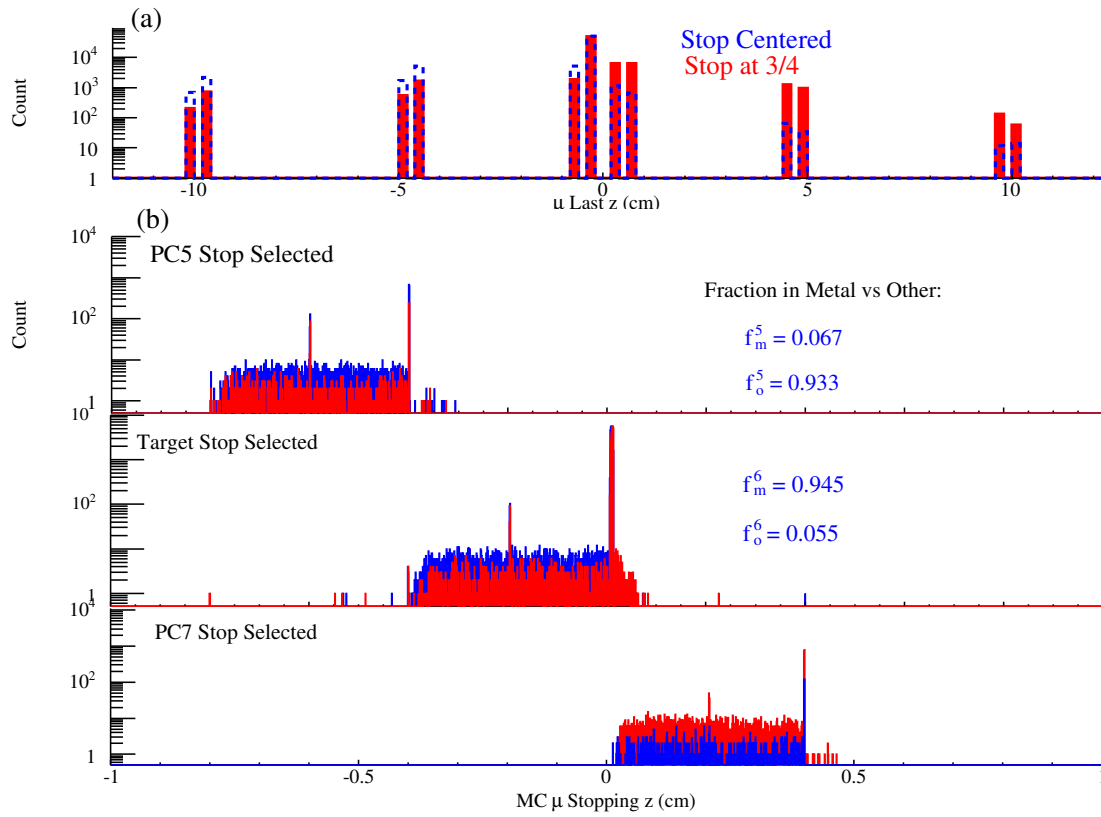


Figure 6.5: (a) The simulated distribution in z coordinate of muons stopping in chambers around the muon stopping target. (b) Expanded view of the muon stopping z coordinate for selection of PC5, PC6 and PC7 as the last plane hit by the muon. The last hit in PC5 is at top, PC6 is in the middle, and PC7 is at bottom. In both (a) and (b) muons with the Bragg peak centered in the muon stopping target are shown in blue, and those stopping at 3/4 are shown in red.

By knowing the fraction of muons stopping in each material and measuring P_μ from the muon decay spectrum from different selections of the muon's last plane hit, we can estimate the level of this effect. The fraction of muons stopping in different materials depends on where the muon Bragg peak is centered. The stopping fraction in different materials when the muon's last hit occurred in PC 6 is shown in Figure 6.6. The fraction stopping is plotted versus the mean muon stopping position.

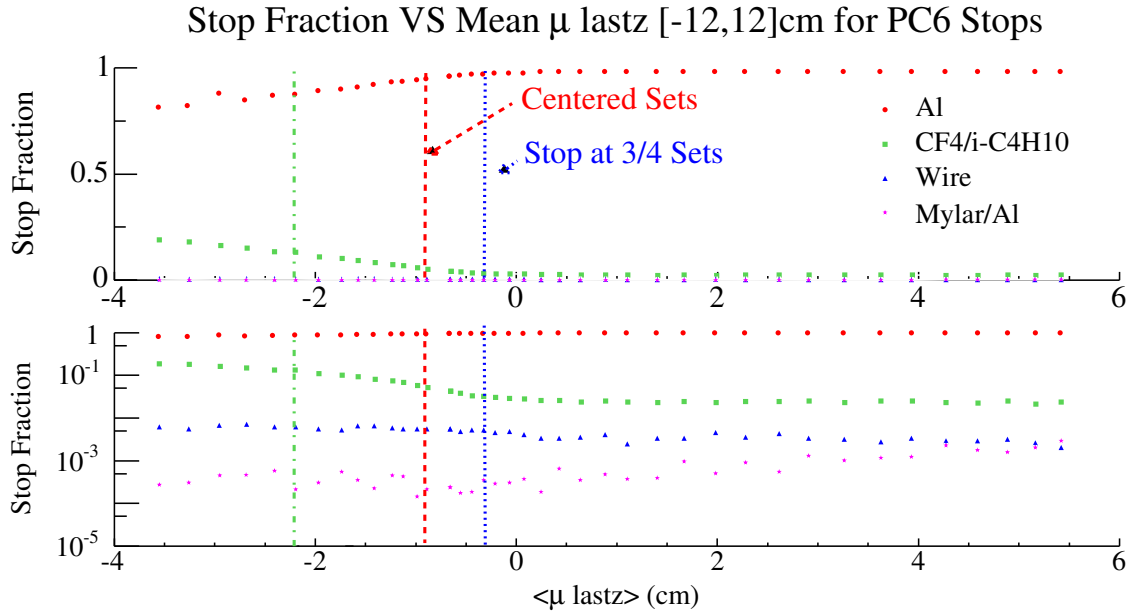


Figure 6.6: Fraction of muons stopping in aluminum (Al), gold plated tungsten wire, CF4/i-C4H10, and aluminized Mylar foil for muons with last plane hit in PC6, versus the mean muon stopping z coordinate between -12 cm and 12 cm from the last plane hit information. The mean muon stopping z coordinate for: data set 32 is shown as a green line, data sets with the Bragg peak centered as a red line, and the data sets stopping at $3/4$ as a blue line.

MDSL: Estimate from Extrapolation Error

A decay time dependency of the depolarization was observed for muons stopping in an Al target. Plots of the polarization estimate from an asymmetry analysis of the 2004 data and simulation are shown in Figure 6.7. A Gaussian depolarization with a sigma of $54.4 \mu\text{s}$ was included in the simulation to match the observed depolarization in 2004 data. A Gaussian form was chosen before it was decided that only an exponential form was possible. The difference in shape between a Gaussian and an exponential for decay times from 1050 ns to 9000 ns is indistinguishable at the level of statistics used in this measurement. Note that the average spin from muon stops is known exactly in the simulation so this error can be corrected.

The depolarization rate cannot be explained solely by muons that stop in gas rather than in Al. Models for depolarization in metal are either of an exponential or Gaussian form. However, calculations shown earlier in this section imply that the only practical form is an exponential shape in Al since the effects of the other models are very small.

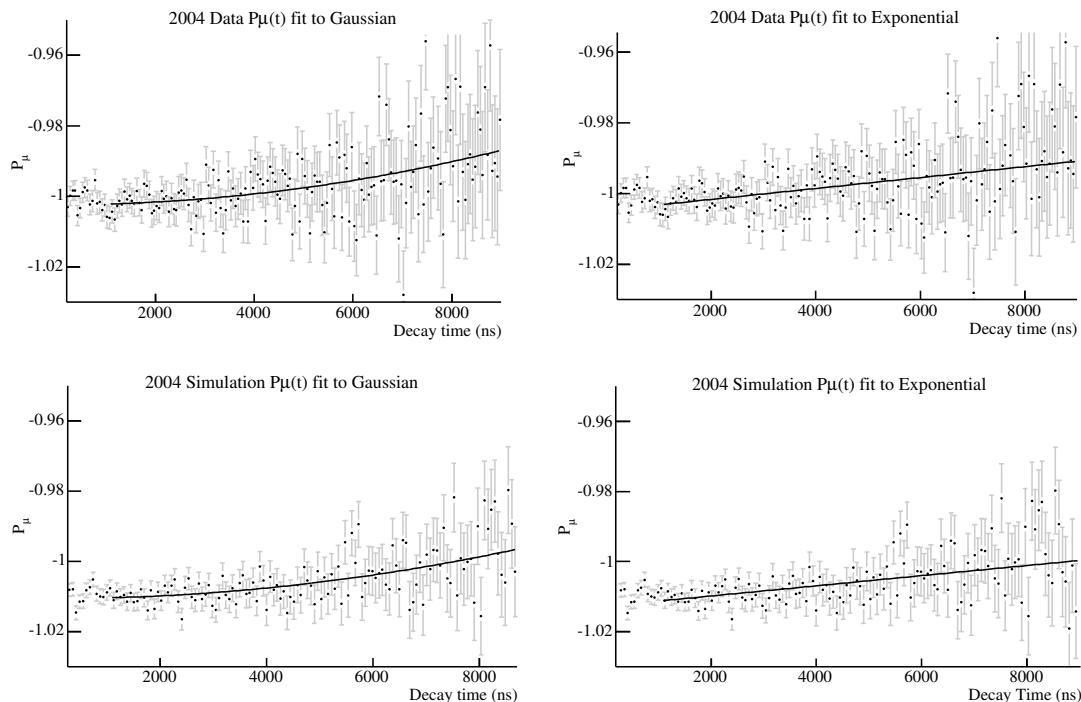


Figure 6.7: Polarization estimate from an asymmetry analysis of the 2004 data at the top, and 2004 simulation at the bottom. The distributions are fit to a Gaussian on the left and to an exponential on the right. The fit excludes decay positrons before a decay time of 1050 ns to avoid the potential bias from extra muon hits in the upstream decay positrons.

Jodidio *et al.*, measured a depolarization rate of $(-0.43 \pm 0.34) \times 10^{-3} \mu\text{sec}^{-1}$ for their Al target at 1.1 T [45]. This rate is about 3.5 times smaller than the $(-1.55 \pm 0.28) \times 10^{-3} \mu\text{s}^{-1}$ for our muon stops. The difference in rate is attributed to the 2.5 to 5.5% of the muons that stop in the gas before our stopping target. Attempts were made to determine separate slopes for our Al and gas depolarizations, but this did not work well because the method was too sensitive to the exact shape of the stopping distribution. Since about 2/3 of our depolarization must come from the gas stops it is uncertain whether the shape of the depolarization is Gaussian or exponential.

The difference between the two model extrapolations is 2.4×10^{-3} . Half of the difference is the *correction* applied to simulation to data fits, since the simulation was generated with a Gaussian form, while in reality the shape is most likely something between Gaussian and exponential. An estimate of the extrapolation uncertainty is $\sqrt{2}$ times the extrapolation

uncertainty. The uncertainty in $P_\mu\xi$ due to extrapolation is: $\pm\sqrt{2}(0.00099) = \pm 1.4 \times 10^{-3}$.

6.1.5 Background Muon Contamination

Another contribution to the depolarization is contamination from “background” muons. Strong evidence for muons with a different polarization and longer range than surface muons is found in the 2002 data where the muons were stopped further upstream than the nominal target position. In this set a reduced polarization is observed for those muons whose last hit was in PC7 or PC8.

It is expected that nearly all of the surface muons will stop by the end of the target module. Stops observed further downstream than PC7 and PC8 have a probability, increasing with plane number, of being due to the “background” muons. An estimate for the contamination is made in the following way. The data were modeled in GEANT as a combination of a standard GEANT run with polarized surface muons, and a special run with muons arising from 29.6MeV/c pion decays in the M13 channel and beam package area upstream of the TWIST chambers. Figure 6.8 shows the distributions of muon last plane hit for data and simulation before and after adding pions to the beam.

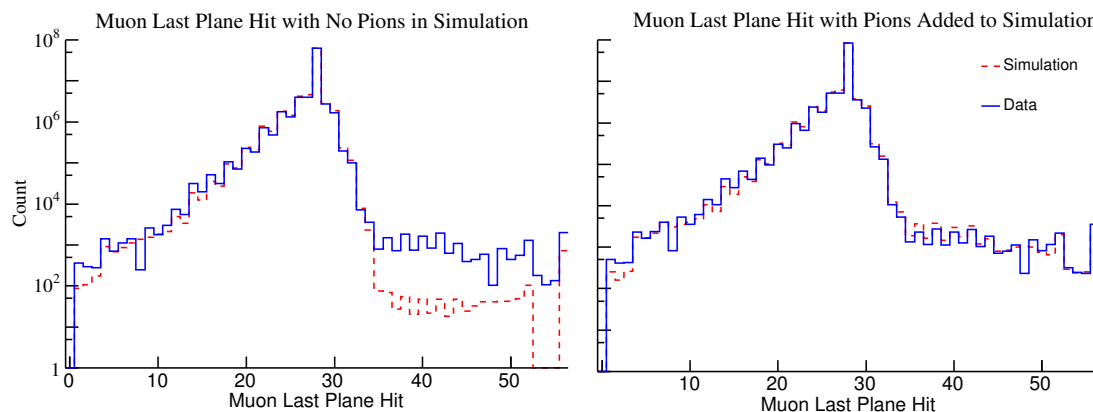


Figure 6.8: Overlay of the data set 35 and matching simulation last plane hit histogram before adding muon stops from pions in the beam on the left. The same histograms but with pions added at to the simulation to match the data is shown on the right.

The fraction of muon stops due to the pions relative to surface muons is summarized for the 2002, 2003, and 2004 data in Table 6.5. The maximum polarization change is calculated for the case where the background muons have polarization opposite to surface muons. These estimates show that the systematic uncertainty in $P_\mu\xi$ due to background muons in the 2003 and 2004 data is less than ± 0.00018 .

Data Type	f_{PC5}	f_{target}	f_{PC7}	$\max \Delta P_\mu$
2002 Nominal (Set 2)	0.009106	0.000364	0.000669	0.00072
2002 Upstream (Set 4)	0.009027	0.002793	0.012078	0.00240
2003 Nominal (Set 14)	0.000134	0.000013	0.000040	0.00003
2004 Nominal (Set 35)	0.001110	0.000088	0.000798	0.00018

Table 6.5: Fractions of background muons relative to surface muons for muons stopping in PC5, the target, and PC7. For the target stops the maximum effect on the polarization is estimated.

6.1.6 Beam Intensity and Coincident Accidental Particles

To estimate a systematic uncertainty in $P_\mu \xi$ due to beam rate and coincident particles the 2002 data was used. A spectrum fit of low rate data with a muon rate of 1.18 kHz to high rate data with a muon rate of 4.7 kHz yielded a sensitivity in $P_\mu \xi$ of $(-3.0 \pm 1.7) \times 10^{-3}$.

For the 2004 data sets the rate was about 3 kHz. The largest RMS beam rate was 215Hz from data set 37. Although accidentals have a quadratic dependence, the rate of accidentals in coincidence with a trigger has a linear dependence. The scaling of the sensitivity is also assumed to be linear. The scale factor is the ratio of the changes in beam rate: $\frac{3.5}{0.215} = 16.3$. The systematic uncertainty in $P_\mu \xi$ due to beam intensity is therefore 0.18×10^{-3} .

6.1.7 Proton Beam Stability

The effect of muon beam movement as the proton beam on the production target was moved was also considered. The result is that $\langle dy_\mu \rangle / dy_p \approx 0.25$, and $\langle dx_\mu \rangle / dx_p \approx 0.5$. Movement of the proton beam by ± 1 mm resulted in a change in the muon beam angle $\langle dx \rangle$ of 0.2 mrad, and the change in $\langle dy \rangle$ of 1.3 mrad

Monitoring of the beam position is done using roughly weekly low intensity target scans, where about $1 \mu A$ of proton beam is steered both vertically and horizontally. Vertical steering of the protons is done with steering magnet labeled 1ASM4 (SM4), and horizontal steering with 1ASM5 (SM5). The calibration of the movement of the beam is with “protect monitor” plates located 2.5 mm to either side of the nominal proton beam path. The setting of these steering magnets is monitored in our slow controls. The variation in position of the proton beam over the production data taking period estimated from these history plots is 0.25 mm vertically and 0.1 mm horizontally.

From these numbers, the maximum movement of the muon beam due to proton beam movements is 0.063 mm vertically and 0.025 mm horizontally. The change in angle of the muon beam due to the movement of the proton beam is within 0.08 mrad vertically and 0.01 mrad horizontally. The final result is that the systematic uncertainty due to the proton beam stability is $\pm 0.02 \times 10^{-3}$.

6.2 Systematic Uncertainty Due to Chamber Response

This section describes the systematic uncertainty due to the drift and proportional chamber response. Six sources are considered: time variations in the wire to wire timing (t_0 variations), changes to the space-to-time relations (STR) from density variations, foil bulge due to changes in differential pressure between the chamber gas and He volume, the asymmetry of the wire positions relative to the foils due to construction, dead-zone due to a recovery time after a muon passes through the chambers, and a difference in the upstream versus downstream chamber efficiency.

Two other effects that were considered, but not included in the final estimate of the systematic uncertainty were a corner of the cell drift time uncertainty, and cross talk removal. They were not included because they were measured to be negligible, or would introduce double counting.

6.2.1 Wire to Wire Time Variations

To estimate the possible time variation in the wire to wire time zero, calibration runs were taken at the beginning and end of the run period. The beginning and end calibration runs were taken with the magnetic field off with a single trigger. From these calibration runs two different calibration files were made. The end of run time calibration run was done after a disaster that disabled half of the chambers. For the end of run calibration file the times for the missing planes used times from a different beginning of the run time calibration.

To measure the sensitivity of the muon decay parameters to t_0 variations, a calibration file scaled by ten times the difference in the beginning and end of run time calibrations was used. The large changes in time calibrations caused the helix track fits have much worse χ^2 . The change in $P_\mu\xi$ obtained from fitting the exaggerated time shift analysis spectrum to a normal analysis spectrum was $(8.9 \pm 0.9) \times 10^{-3}$. The resulting systematic uncertainty is 0.89×10^{-3} . A second sensitivity with a calibration file scaled by 5 times the difference in beginning and end of run showed that this systematic uncertainty scales linearly.

6.2.2 Chamber Foil Bulge

The shape of the chamber cathode foils depends on the differential pressure between the chamber gas and the He gas of the cradle holding all of the chambers. The differential pressure of the chambers was monitored and controlled by the gas system. To measure the level of foil bulge, several nominal data runs were taken at different differential pressures. The average helix fit drift time difference for tracks that go through the center of the chambers relative to the average helix fit drift times for tracks that go through the radially distant part of the chamber was found to be sensitive to the foil bulge. Run to run monitoring of this fit time difference shows that the variation in foil bulge was controlled to better than $50 \mu\text{m}$.

To measure the sensitivity of the muon decay parameters to the chamber foil bulge a simulation set was generated with the STR calibration changed as if the foils were moved outward by $500 \mu\text{m}$. A fit of the decay positron spectrum from this exaggerated bulge to a nominal decay positron spectrum yielded a change in $P_\mu\xi$ of $(2.2 \pm 1.4) \times 10^{-3}$. The systematic uncertainty due to time variations in the foil bulge is estimated to be 0.22×10^{-3} .

6.2.3 Chamber Cell Asymmetry

Surveys of the constructed chambers show that the spacing between the wire plane and cathode foils was not the same on both sides of the wire. On average the cathodes were found to be shifted by about $150 \mu\text{m}$ from their nominal 2 mm spacing from the wire planes. With the magnet on, the position of the cathode foils was also determined using normal decay positron data. Using the bulge calibration data from runs with different bulges a relationship between a time difference to a foil shift was obtained. The time difference used for the cathode foil position estimate was the difference between the average helix fit time in one half of the chamber cell to the average time in the other half of the chamber cell.

To investigate the effect of these cathode foil shifts, the foil shifts *measured in software* were simulated in simulation. STR files were changed half-plane by half-plane to match the measured shifts. A fit of the muon decay distribution from the shifted cathode foil simulation set to a simulation set with symmetric planes gave a change in $P_\mu\xi$ of $(-0.2 \pm 1.4) \times 10^{-3}$. Since this shift of the cathode foils is thought to match the real detector, there is no scaling of this sensitivity. The sensitivity is used as the systematic uncertainty.

6.2.4 Density Variations

History plots of the density variation for each 2004 data set show that the largest RMS change in density was $\pm 0.7\%$ from data set 38. To estimate the effect of density changes a simulation set was generated with the temperature changed by 10% (from 300 K to 270 K) to give a scaling factor of 14.3. The muon stopping distribution was not adjusted to compensate for the change in density so there is some double counting. Since this systematic uncertainty is small the stopping distribution contribution was not included. A fit of the changed temperature simulation set to a nominal simulation set gave a change in $P_\mu\xi$ of $(2.4 \pm 1.4) \times 10^{-3}$ which translates to a systematic uncertainty of 0.17×10^{-3} .

6.2.5 Muon Dead-zone

As the muon passes through the upstream half of the detector, before coming to a stop in the stopping target, it deposits large ionization in the chambers. The resulting electron avalanches near the wires take time to recover as the positive ions drift back to the cathode planes. These dead zones only affect decay positrons that go upstream and pass near where the muon made hits in the chambers. The muon dead-zone therefore causes an upstream-downstream efficiency difference for decay positrons. The dead-zone was measured by projecting helical fits to the decay positrons back to a wire that had a muon hit. For each muon hit the wire efficiency versus distance away from the muon hit is estimated as a function of time after the muon track. The dead-zone measured in the data had a lifetime of $3 \mu\text{s}$, and its size was 0.056 cm for the DCs and 0.146 cm for the PCs.

A measurement of the muon decay parameter sensitivities to the muon dead-zone was made by introducing a dead-zone with $\sigma = 5 \text{ cm}$ and exponential lifetime of $3 \mu\text{s}$ for both the PCs and DCs. A fit of this exaggerated dead-zone decay positron simulation to a spectrum from a simulation run with no dead-zone yielded a change in $P_\mu\xi$ of $(0.2 \pm 1.4) \times 10^{-3}$.

To determine the scaling of the sensitivity a small statistics simulation with the dead-zone as measured in data was done to count the number of decay positron hits removed by the dead-zone. The number of hits removed from the exaggerated dead-zone simulation was also counted, and the estimate of the scaling was the ratio of the hits in each of these runs. The resulting scaling factor was 11.7 for the PC where the muon stops, 25.8 for the DCs, and 47.6 for the far upstream PCs. A conservative estimate of the systematic uncertainty due to the muon dead-zone is 0.01×10^{-3} using the scaling factor of 11.7.

6.2.6 Upstream versus Downstream Efficiency

The difference in the average number of degrees of freedom in the track fits in the upstream versus downstream directions for tracks with the same energy and angle is used to estimate an upstream/downstream efficiency difference. The difference between the upstream and downstream average number of degrees of freedom in data versus simulation is 0.18. The average data and simulation degrees of freedom for different decay positron momenta and angle are shown in Figure 6.9.

To estimate the sensitivity of the muon decay parameters due to a difference in upstream versus downstream efficiency a data set was analyzed with 5% of its downstream DC hits thrown away at the unpacking stage of the analysis. This upstream downstream inefficiency change compared to a normal analysis of the same data gave a sensitivity of $(1.9 \pm 0.9) \times 10^{-3}$, where the error in the sensitivity was rescaled since the fit was correlated.

The lowered efficiency run has about 1.8 NDOF less downstream compared to the standard run. Given that the difference between simulation and data is 0.18 NDOF the scaling of the sensitivity is 10; the systematic uncertainty due to the difference in upstream and downstream efficiency is ergo 0.2×10^{-3} .

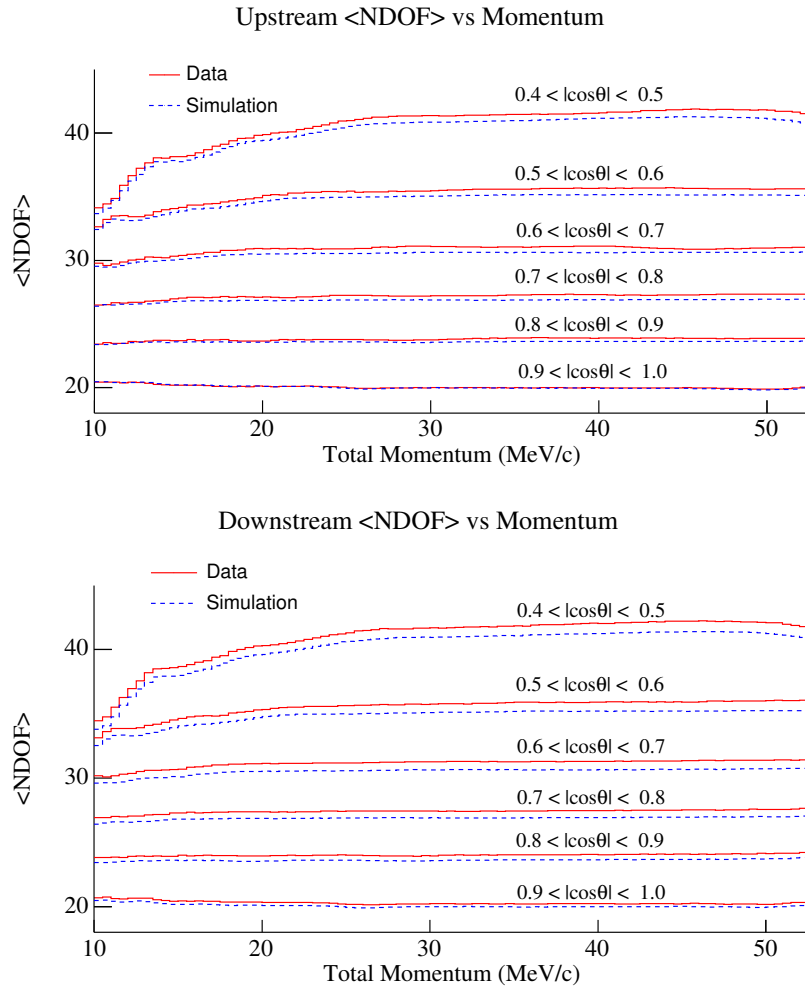


Figure 6.9: Mean helix fit number of degrees of freedom (NDOF) versus momentum for different ranges of $\cos \theta$. The blue dashed line of each $\cos \theta$ range is from simulation, and the red solid line is the data. The distributions for upstream decays are shown in the top plots, and the downstream decays are shown in the bottom plots.

6.3 Systematic Uncertainty Due to Momentum Calibration

The systematic uncertainty in the momentum calibration comes from two contributions. One contribution is due to how well we can do our endpoint energy calibration. The other factor is how well our measured magnetic field map represents reality.

6.3.1 Endpoint fits

The method of doing endpoint fits to obtain a momentum calibration is presented in Section ???. The sensitivity to the momentum calibration is measured by fitting a decay positron spectrum that has the momentum calibration properly applied to a spectrum where one of the energy calibration parameters (α_u , α_d , or β) was shifted by 100 keV/c. When measuring the sensitivity to β , the values of α_u and α_d were changed to follow the correlation observed in Figure ??.

With the end point β fixed to zero, the uncertainty σ_i for β is obtained from the discrepancy of 2 G in 20000 G in the shape of the field map in the tracking region. This gives an uncertainty at the endpoint momentum in β of 5.3 keV. Endpoint fits with β fixed have uncertainty in α of about 1 keV/c, as summarized in Section ???. The sensitivity, scaling factor, and systematic uncertainty contribution from each of the energy calibration parameters is summarized in Table 6.6. The resulting systematic uncertainty in $P_\mu\xi$ is 0.16×10^{-3} .

Parameter	Sensitivity		Scale R_i/σ_i	Systematic Uncertainty
	S_i value	S_i error		
α_u	-15.75	0.08	100	0.16
α_d	0.649	0.004	100	0.01
β	-0.46	0.31	20	0.02
Total				0.16

Table 6.6: Energy calibration sensitivities and systematic uncertainties in units of $\times 10^{-3}$. The total is the quadrature sum of the individual systematic uncertainties.

6.3.2 Magnetic Field Uniformity

Inaccuracies in the magnetic field map lead to inaccuracies in the determination of the decay positron momentum. To quantify this effect, a modified magnetic field map was produced by distorting the standard field simulation as follows:

$$\Delta B_z = -(0.006 \text{ G/cm}^2) z^2 - (0.00004 \text{ G/cm}^3) z^3 - (1.25 \text{ G/cm}) r \quad (6.6)$$

A nominal data set was analyzed with the distorted field map, and the resulting decay positron spectrum was fit to the standard analysis of the same data set. The resulting sensitivity to $P_\mu\xi$ was $(-0.9 \pm 1.6) \times 10^{-3}$.

The distorted field map differs from the nominal 2 T field map by up to 40 G at the extremes of the tracking volume. Differences between an Opera generated field map, and the

measured field map are 2 G at the extremes of the tracking region. A conservative scaling factor of 10 gives a systematic uncertainty in $P_{\mu\xi}$ of 0.09×10^{-3} .

6.4 Systematic Uncertainty Due to Positron Interactions

The systematic uncertainty due to positron interactions includes four effects: a discrepancy between the simulation and data energy loss, hard and intermediate interactions, multiple scattering, and back-scattering from material outside our detector. A systematic uncertainty due to the target thickness is described, but not included in the final table of systematic uncertainties because its contribution is negligible.

6.4.1 Energy Loss

The energy loss systematic effect has to do with an unexplained difference of 7 keV/c between our simulation and data energy loss at the endpoint momentum. This 7 keV/c difference was measured using a special data set where muons were stopped upstream in the trigger scintillator and the first four PCs. The decay positrons that went downstream through all of the DCs were then fit twice with our helix fitting code; once to the upstream half of the track and once to the downstream half of the track. The difference in momentum between these two track fits is called Δp in this section.

The systematic uncertainty estimate comes from looking at the difference in slope between data and simulation in a $(\Delta p) \cos \theta$ versus p using this special data set as shown in Figure 6.10. The difference in slope is $(7 \text{ keV/c}) / (50 \text{ MeV/c}) = 1.4 \times 10^{-4}$.

To obtain the sensitivity to a difference in the slope defined as α_1 in Section ??, an energy calibration with $\alpha_1 = 0.014$ was performed giving a scaling factor of 100. The sensitivity after rescaling the error (since the fit was correlated) was $(0.64 \pm 0.20) \times 10^{-3}$, giving a systematic uncertainty in $P_\mu \xi$ of 0.01×10^{-3} .

6.4.2 Hard and Intermediate Interactions

One of the positron interaction systematic uncertainties has to do with how well we can validate the simulation of hard and intermediate interactions. Hard interaction events are arbitrarily defined here to be events in which the decay positron loses more than 1 MeV/c of momentum from where it is generated to where it goes through the last DC. Intermediate interactions are those events whose decay positrons have lost less than 1 MeV/c.

In our simulation we can look at the ratio of the reconstructed decay positron distribution and the thrown distribution to see how large a correction factor is needed to account for hard and intermediate interactions. The ratio of reconstructed over thrown distributions in $\cos \theta$ for all events, events that lose $< 1 \text{ MeV/c}$, and those events that lose $> 1 \text{ MeV/c}$ is shown in Figure 6.11.

Muon decay spectrum fits of the reconstructed to thrown distributions for all events, and for events that lose less than $< 1 \text{ MeV/c}$ were done to estimate the size of correction. Plots of the change in $P_\mu \xi$ are shown in Figure 6.12. Note that the sign needs to be flipped for the systematic because of the order in which the fit was done.

Fits of the hard interactions to the thrown distributions failed because the shape of the distribution was too different from that of the muon decay spectrum shape. To estimate the hard interaction contributions, the difference between fits to all events and fits to intermediate events is considered. Since this estimate is not very robust, a different method for obtaining

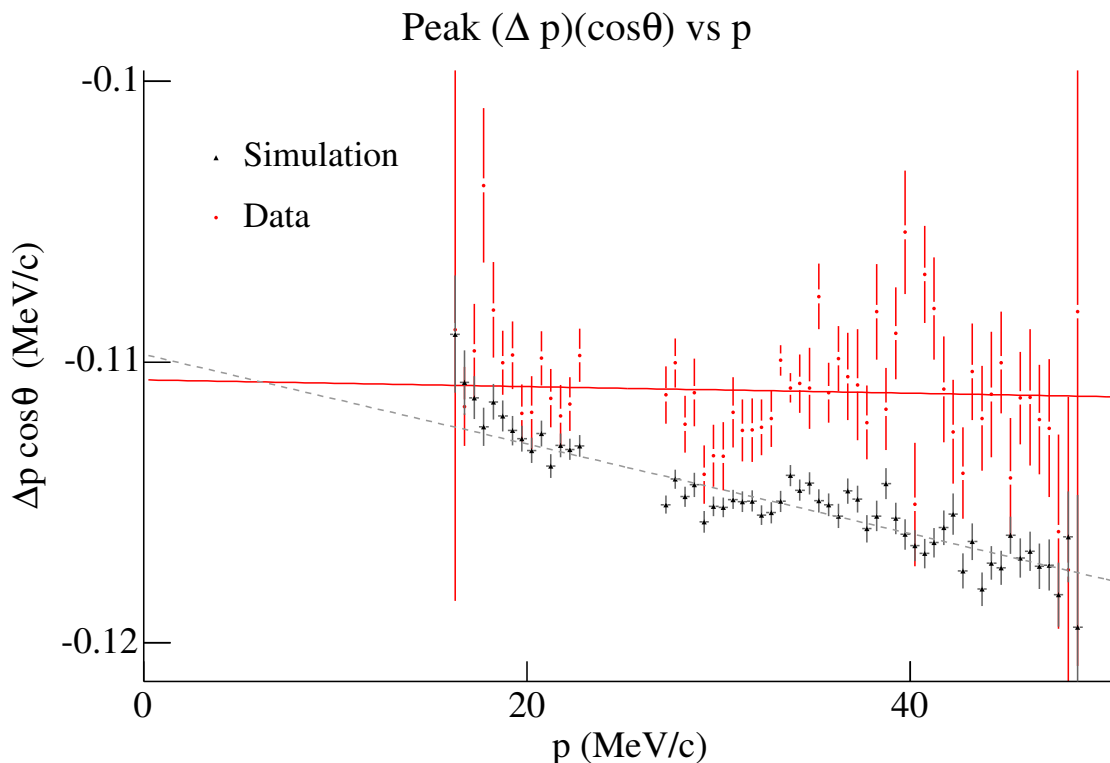


Figure 6.10: Comparison of $\Delta p \cos \theta$ versus p in Data and simulation. Δp comes from the difference in upstream and downstream fits to positrons from a data set with muon stopping upstream in the trigger scintillator and PCs.

the final systematic uncertainty is described near the end of this section. The size of the corrections from the fit results are listed in Table 6.7 for $P_{\mu\xi}$. The size of the correction depends on the location of the muon stopping Bragg peak in the stopping target.

The hard interaction systematic uncertainty is estimated using a fit of a nominal simulation set, to a simulation set where the cross section for Bremsstrahlung was increased by ten times. In this fit $P_{\mu\xi}$ was shifted by $(17.9 \pm 1.4) \times 10^{-3}$. Using the 5% discrepancy in hard interactions estimated in Section ??, the the scaling factor for this sensitivity is $10/0.05 = 200$. This gives an estimate of $(0.09 \pm 0.01) \times 10^{-3}$ for the systematic uncertainty in $P_{\mu\xi}$ due to hard interactions.

Given that our simulation is validated to 5% for intermediate interactions, and using a systematic uncertainty in hard interactions of 0.00009, we obtain a systematic uncertainty in $P_{\mu\xi}$ of:

$$\begin{aligned} &0.63 \times 10^{-3} \text{ for PC5 stops,} \\ &0.35 \times 10^{-3} \text{ for centered stops, and} \end{aligned}$$

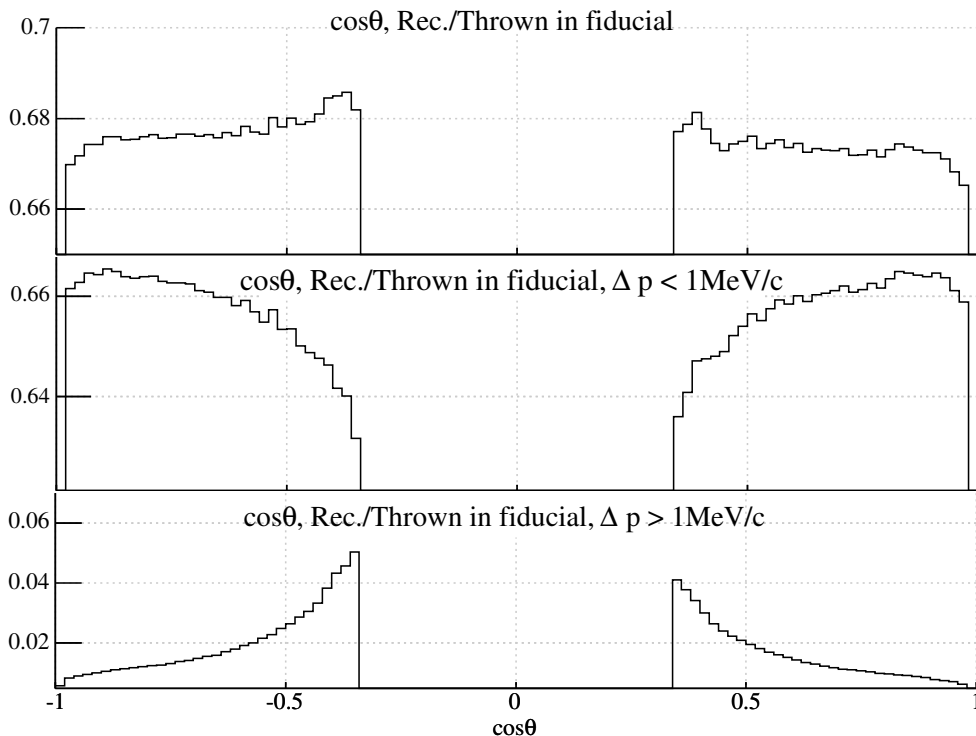


Figure 6.11: Reconstructed over thrown yield versus $\cos\theta$ for events in the fiducial $p_{total} < 50.0$ MeV/c, $p_{\perp} < 38.6$ MeV/c, and $p_z > 13.7$ MeV/c. The top plot is for all events, the middle plot is for events where the decay positron loses less than 1 MeV/c, and the bottom plot is for positron energy loss greater than 1 MeV/c. The plots are for a muon stopping distribution centered in the target.

0.12×10^{-3} for stops at 3/4.

An average systematic uncertainty in $P_{\mu\xi}$ weighted by the number of datasets with each stopping distribution is 0.29×10^{-3} . For plots and a description of the validation of our simulation refer to Section ??.

6.4.3 Multiple Scattering

The sensitivity of $P_{\mu\xi}$ to multiple scattering was measured by smearing the reconstructed positron angle in the analysis of a standard simulation set. This smearing took the form:

$$\Delta\theta = \frac{k}{|\vec{p}|\sqrt{\cos\theta}} \quad (6.7)$$

The resulting decay positron spectrum was fit to the unsmearred spectrum from the same simulation set yielding a sensitivity of $(-3.2 \pm 1.4) \times 10^{-3}$.

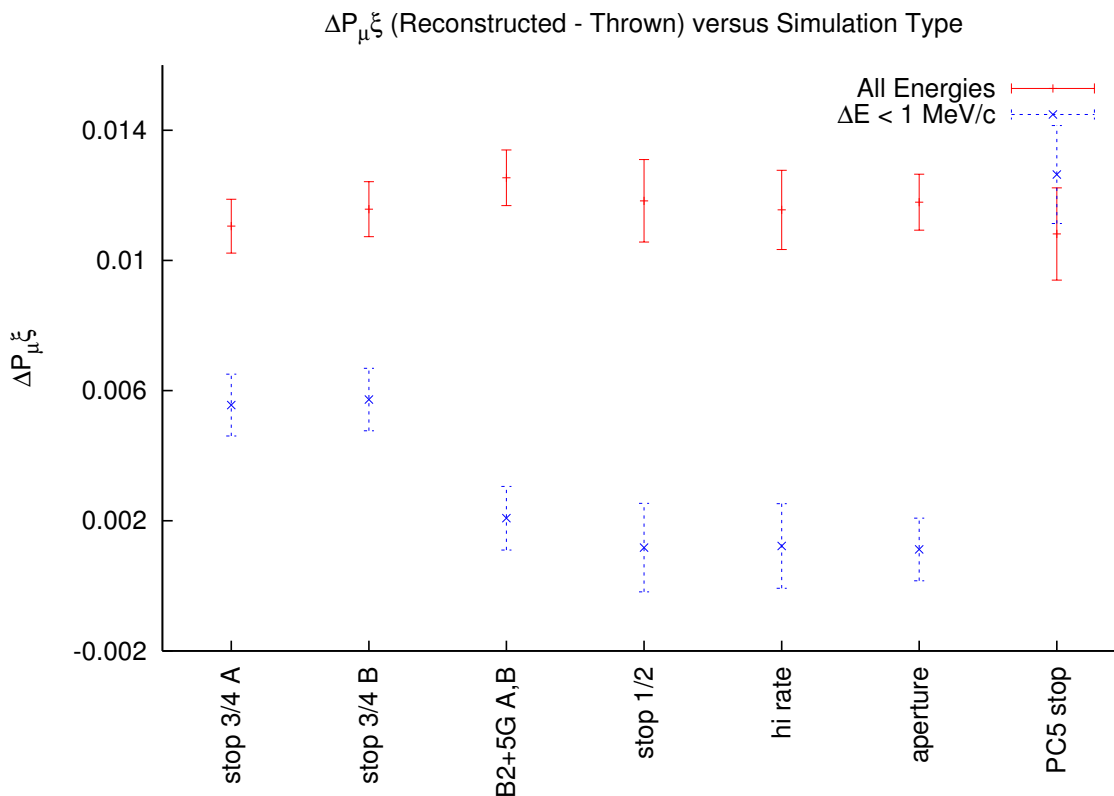


Figure 6.12: $\Delta P_{\mu\xi}$ from spectrum fits to distributions of $\cos\theta$ versus total momentum of reconstructed to thrown decay positron distributions. Michel fits to all events are shown as '+' and the fits to events with decay positrons that lose less than 1 MeV/c are shown as 'x'. Points 1 and 2 are for muons stopping centered, points 3 to 6 are stopping at three-quarters, and point 7 is for muons stopping further upstream.

The inaccuracy in the simulation of multiple scattering is 0.7 mrad as described in Section ???. The constant k was chosen so that a typical 30 MeV/c momentum track at 45° had a $\Delta\theta$ of 30 mrad. The systematic uncertainty is -0.08×10^{-3} .

6.4.4 Material Outside the Detector

Materials outside the tracking volume acted as surfaces for the decay positrons to undergo a back-scattering. In particular, components of the beam package were a source of deltas and backscatters caused by a decay positron. The systematic uncertainty due to such extra particles was calculated by collecting a set of data with additional material introduced downstream of the detector.

The spectrum from a data set with extra material was fit to a spectrum from a data set without the extra material yielding a change in $P_{\mu\xi}$ of $(1.2 \pm 2.0) \times 10^{-3}$. The extra

μ Location in Target	$\Delta P_{\mu\xi}$ Inter.	$\Delta P_{\mu\xi}$ Hard
PC 5 stops (upstream)	-0.0125	0.0015
centered ($\frac{1}{2}$)	-0.0068	-0.0037
$\frac{3}{4}$	-0.0015	-0.0105

Table 6.7: $\Delta\xi$ corrections due to intermediate and hard interactions for each of the three different muon stopping locations of data.

material added was an 0.65 cm thick aluminum plate mounted on an 0.59 cm thick plastic plate about 80 cm downstream of the central stopping target. The effect is scaled by the ratio of extra particles due to the aluminum divided by the difference between data and simulation in nominal conditions.

$$\frac{R_i}{\sigma_i} = \frac{N_{Al}^{Extra\ Particles}}{|N_{Data}^{Extra\ Particles} - N_{Simulation}^{Extra\ Particles}|} = 60 \quad (6.8)$$

The resulting systematic uncertainty is 0.02×10^{-3} . Note that outside the nominal fiducial region differences between the simulation and data backscattering have been observed. The difference is predicted to be due to backscattering from the solenoid yoke which was not present in the production simulation. Plots showing the distribution of decay positron angle and energy for events identified as having a backscatter or beam positron correlated in time with the decay positron are shown in Figure 6.13.

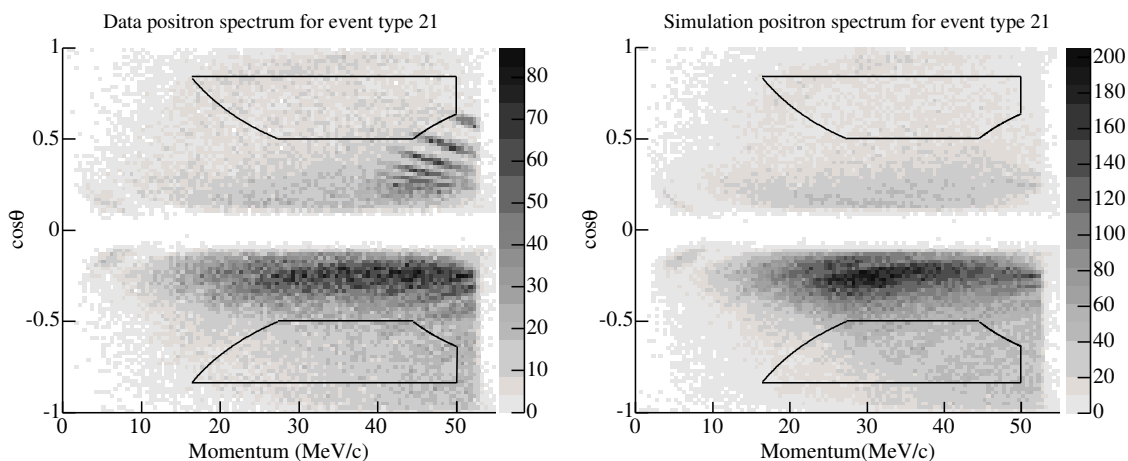


Figure 6.13: Distribution of decay positron $\cos\theta$ versus total momentum in MeV/c for events identified as having a backscatter or beam positron correlated in time with the decay positron. The top two plots are two different backscatter event types from data, and the bottom two plots are the same event types from the simulation.

6.4.5 Stopping Target Thickness

The muon stopping target is $71 \pm 1 \mu\text{m}$ of high purity Al. The systematic effect due to the $1 \mu\text{m}$ uncertainty is approximated using a simulation generated with a $125 \mu\text{m}$ Mylar stopping target with graphite layers of $30 \mu\text{m}$ on each side. The resulting decay spectrum was fit to a spectrum created with $10 \mu\text{m}$ layers of graphite. Using the very rough approximation that the extra $40 \mu\text{m}$ of graphite is equivalent to $40 \mu\text{m}$ of Al, this corresponds to a scaling factor of 40. The resulting target thickness systematic uncertainty in $P_{\mu\xi}$ is $(0.02 \pm 0.03) \times 10^{-3}$.

6.5 Systematic Uncertainty Due to Spectrometer Alignment

The following subsections describe and quantify the systematic uncertainties related to the spectrometer alignment. The systematic uncertainty due to spectrometer alignment comes from: how well the chamber translations in x, y, z and angle are corrected to match their true positions, and the degree to which the misalignment between the magnetic field axis to the chamber axis is treated.

6.5.1 Longitudinal Alignment

The alignment of the planes in z is by construction. The spacing of the chambers was precisely measured and controlled by the special Sital spacers. The precision of the chamber spacing is $30\ \mu\text{m}$ longitudinally. To measure the sensitivity of the muon decay parameters to a longitudinal misalignment of the chambers, random offsets of ten times the chamber spacing precision were introduced in the analysis of a simulation set. The resulting systematic uncertainty in $P_{\mu}\xi$ is 0.22×10^{-3} .

6.5.2 Rotational Alignment

The rotational alignment systematic was found by analyzing a data set with an alignment file containing random rotational offsets 10 times the 0.01° precision of the rotational alignment corrections. The systematic uncertainty in $P_{\mu}\xi$ due to the rotational alignment is 0.22×10^{-3} .

6.5.3 Magnetic Field Alignment

The accuracy of the alignment of the magnetic field axis to the chamber axis is 0.02 mrad, but the mismatch between upstream and downstream is 0.1 mrad for the 2004 data.

To measure the sensitivity a misalignment of the magnetic field of 0.25 degrees (4.4 mrad) was introduced in the simulation. A fit of the reconstructed decay positron spectrum of the misaligned simulation to a nominal set gave a sensitivity of $(1.2 \pm 1.4) \times 10^{-3}$.

Using a scaling factor of 40 (4 mrad/0.1 mrad) for the 2004 data gives the systematic uncertainty in $P_{\mu}\xi$ of 0.03×10^{-3} due to the misalignment of the magnetic field.

6.5.4 Translational Alignment

The translational alignment systematic uncertainty was investigated by analyzing a nominal data set with an alignment file containing random translational offsets 28 times the $10\ \mu\text{m}$ precision of the translational alignment corrections. The resulting muon decay spectrum fit yields a systematic uncertainty in $P_{\mu}\xi$ of $< 0.01 \times 10^{-3}$.

6.6 Set Dependent Systematic Uncertainties

The set dependent systematic uncertainties are summarized in this section. Several of the set to set variations were estimated in the relevant sections of this chapter. In several cases

the value is the same for all sets, however those systematic uncertainties are independent set to set. Table 6.8 summarizes the set to set systematic uncertainties.

Effect	Set								
	30	31	32	35	36	37	38	39	
Fringe field depolarization					3.3				
Depolarization at stopping location					1.4				
Background muons					0.18				
Beam intensity	0.04	0.05	0.06	0.17	0.08	0.18	0.04	0.05	
T0 variations					0.89				
Foil bulges	0.22	0.33	0.40	0.20	0.26	0.24	0.33	0.24	
Density	0.06	0.12	0.02	0.06	0.05	0.02	0.17	0.06	
Hard and intermediate interactions	0.37	0.37	0.64	0.37	0.37	0.16	0.16	0.16	
Total in quadrature	3.7	3.7	3.8	3.7	3.7	3.7	3.7	3.7	

Table 6.8: Set dependent systematic uncertainties for each effect and set in units of 10^{-3} . In several cases the value is the same for all sets, however those systematic uncertainties are independent set to set.

Chapter 7

Results

7.1 Blind Fit Results

7.1.1 Blind Fit for $P_{\mu\xi}$

Our datasets alone appear to have no significant difference in polarization according to the asymmetry analysis and Michel fits. The $\Delta P_{\mu\xi}$ value for Michel fits of each 2004 data set to its respective simulation, where the fringe field depolarization was removed from the simulation, is shown in Figure 7.1.

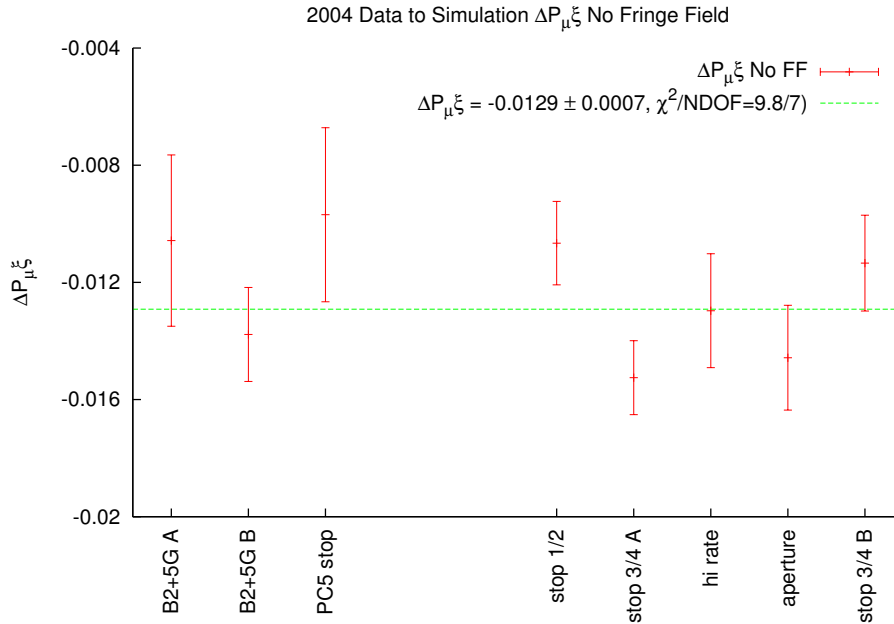


Figure 7.1: $\Delta P_{\mu\xi}$ from 2004 data to simulation Michel fits with fringe field depolarization correction removed from the simulation.

The difference in polarization obtained between the production simulation set with B2+5G and the production simulation set with an aperture inserted is 6.1×10^{-3} . The consistency of the data, and difference in polarization of the simulation is one reason for the conservative estimate in the uncertainty in fringe field depolarization given in Section 6.1.3. The raw $\Delta P_{\mu\xi}$ values from simulation to data fits with the production simulation depolarization values are

shown in Figure 7.2.

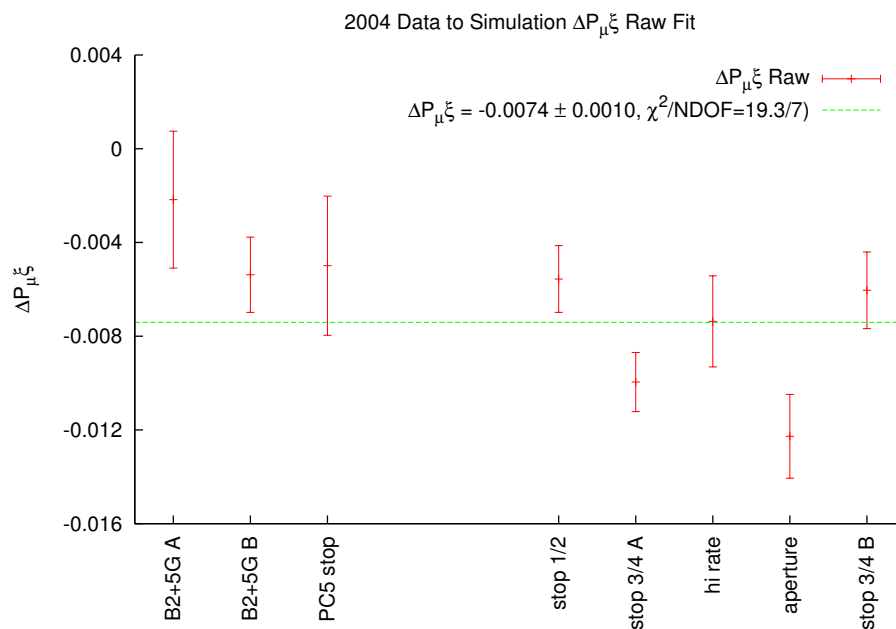


Figure 7.2: $\Delta P_{\mu\xi}$ from 2004 data to simulation fits, with simulation fringe field of production running. Only statistical uncertainties are shown.

A number of corrections need to be made to the polarization used in the production simulation. These corrections are for:

1. an error that shifted the beam profiles by one bin (1 mm) which predicts a slightly different correction, on the order of 0.1×10^{-3} , for each simulation beam
2. ambiguity in the depolarization model choice between Gaussian and exponential depolarization rates (-0.0012) described in Section 6.1.4
3. using the correct beam characterization for each set (-0.0016 to 0.0025)

For the last item, the production simulation was run without the final beam selection so corrections were needed to use the predicted depolarization for the beam measured for each data set. The largest correction is for an error in the selection of the beam tune to use for Set 32. An overall offset in all of the beam depolarization measurements was due to improvements in the TEC calibrations and analysis. The largest differences were from better rejection of multiple tracks with improvements in the TEC analysis code, and the use of a time-of-flight (TCAP) cut to reject beam positrons which had low efficiency for detection but which could leave enough ionization to register false tracks.

The signs of the corrections were determined by deciding if the correction increased or decreased the predicted polarization in the simulation. Since data to data fits say that the

data sets are consistent, taking out the polarization put into the simulation should make the data to simulation fits more consistent as shown in Fig. 7.1. By checking the sign needed to take out the polarization estimated by the simulation, the sign for the corrections was checked.

Table 7.1 gives the raw results of simulation to data fits and the result with corrections applied. A plot of the final corrected values for $\Delta P_\mu \xi$ from the black box value is shown in Figure 7.3. The difference in $P_\mu \xi$ from the black box value is therefore measured to be $(-8.8 \pm 1.1) \times 10^{-3}$. To determine the average difference in $P_\mu \xi$, set to set systematic uncertainties summarized in Table 6.8 were added in quadrature with the statistical uncertainty for each set. The final result is:

$$\Delta P_\mu \xi = (-8.8 \pm 1.1(stat) \pm 3.8(syst)) \times 10^{-3} \quad (7.1)$$

Set	Description	Raw $\Delta P_\mu \xi$	$\chi^2/NDOF$	Corrected $\Delta P_\mu \xi$
30	B2+5G A	-2.2 ± 2.9	1951 / 1887	-4.6 ± 2.9
31	B2+5G B	-5.4 ± 1.6	2017 / 1887	-7.8 ± 1.6
32	PC5 stop	-5.0 ± 3.0	1901 / 1887	-3.7 ± 3.0
35	stop $\frac{1}{2}$	-5.6 ± 1.4	1885 / 1887	-8.2 ± 1.4
36	stop $\frac{3}{4}$ A	-10.0 ± 1.3	1898 / 1887	-12.6 ± 1.3
37	hi rate	-7.4 ± 1.9	1948 / 1887	-10.2 ± 1.9
38	aperture	-12.3 ± 1.8	1904 / 1887	-12.3 ± 1.8
39	stop $\frac{3}{4}$ B	-6.0 ± 1.6	1852 / 1887	-8.6 ± 1.6
Average		-7.4 ± 1.0		-8.8 ± 1.1

Table 7.1: Table of simulation to data $\Delta P_\mu \xi$ fit results in units of $\times 10^{-3}$. The corrected average has $\chi^2/NDOF = 3.8/7$ when including set to set systematic uncertainties.

Fit residuals are reasonably flat inside the fiducial. Fit residuals for the data set with muons stopping centered in the target are shown in Figure 7.4. Residuals for the fits to the other data sets look identical.

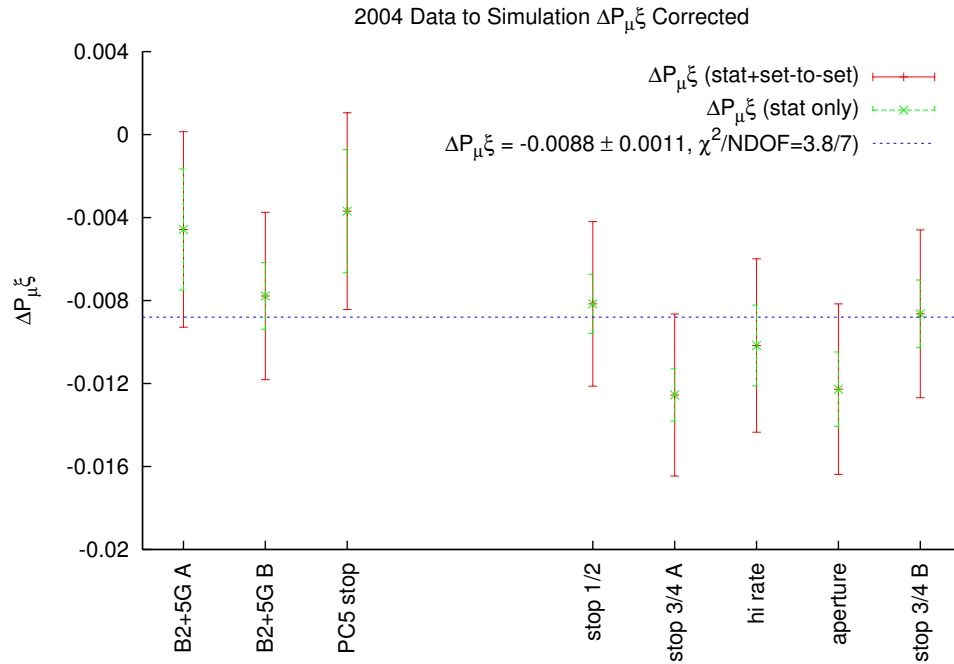


Figure 7.3: $\Delta P_{\mu\xi}$ from 2004 data to simulation fits, with all of the required corrections applied. The smaller error bars are statistical only, and the larger error bars include the set to set systematic uncertainty added in quadrature with the statistically uncertainty.

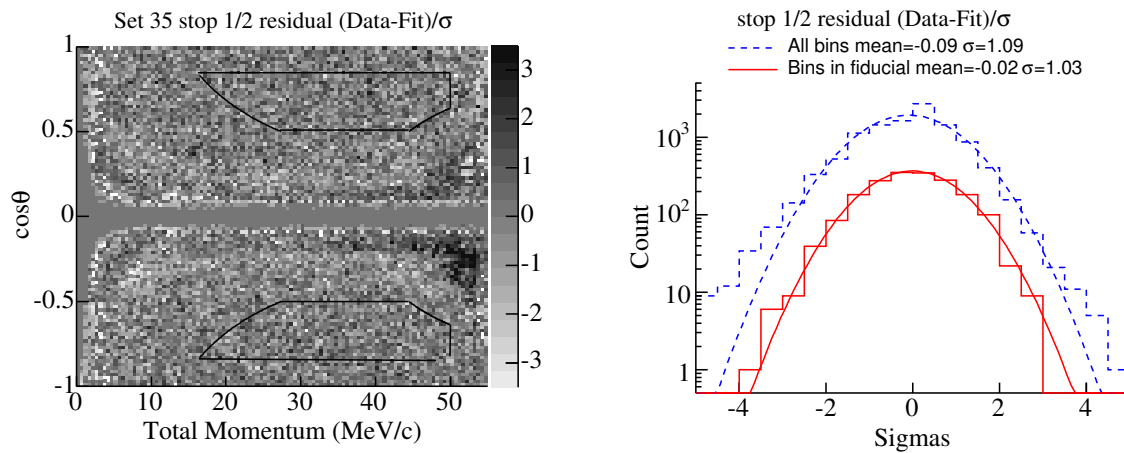


Figure 7.4: Data minus simulation fit residuals, (data-fit)/sigma, for the data set with muons stopping centered in the target. Residuals are plotted for each bin in $\cos\theta$ versus total momentum on the left, and as a histogram on the right. Residuals for the fits to the other data sets look identical.

	ρ	$P_\mu\xi$	$P_\mu\xi\delta$
ρ	1.00	0.31	0.18
$P_\mu\xi\delta$	0.31	1.00	0.41
$P_\mu\xi$	0.18	0.41	1.00

Table 7.2: Correlation coefficients between the spectrum fit parameters.

	ρ	δ	$P_\mu\xi$
ρ	1.00	0.11	0.18
δ	0.11	1.00	-0.56
$P_\mu\xi$	0.18	-0.56	1.00

Table 7.3: Correlation coefficients between the spectrum fit parameters after conversion to the $P_\mu\xi$, δ parameterization.

7.1.2 Blind Fit Results for ρ and δ

Fits to the muon decay spectrum simultaneously measure all of the muon decay parameters. The parameter η was fixed to the black-box value, while the values of ρ and $P_\mu\xi\delta$ were allowed to vary to account for the fairly large correlations between the parameters. The correlation coefficients between the fit parameters are shown in Table 7.2. $P_\mu\xi$ is correlated to both ρ and $P_\mu\xi\delta$ making the three parameter fit desirable.

It is interesting to note that when converting the fit results to obtain the value of δ , there is an anti-correlation between $P_\mu\xi$ and δ . This anti-correlation appears because the value of δ comes from the division of the parameters:

$$\delta = \frac{P_\mu\xi\delta}{P_\mu\xi} \quad (7.2)$$

where the quantity $P_\mu\xi\delta$ has a relatively small uncertainty, and $P_\mu\xi$ has a relatively large uncertainty. The correlation coefficients in the parameters, after conversion to the $P_\mu\xi$, δ parameterization, are listed in Table 7.3.

The average difference from the black-box value of ρ is $(-4.2 \pm 0.3) \times 10^{-3}$, where the consistency of the ρ values between datasets has $\chi^2/NDOF = 8.1/7$. The average difference from the black-box value of δ is $(10.9 \pm 0.6) \times 10^{-3}$, where the consistency of the δ values between datasets has $\chi^2/NDOF = 11.3/7$. The uncertainties reported for ρ and δ are statistical only. These data are being re-analyzed with an improved analysis code to extract more precise values for ρ and δ . Set-to-set values of the deviation of ρ and δ from the black-box value are listed in Table 7.1.2.

Set	Description	ρ	δ
30	B2+5G A	-1.7 ± 1.4	7.3 ± 2.4
31	B2+5G B	-4.4 ± 0.8	10.1 ± 1.3
32	PC5 stop	-2.2 ± 1.5	9.2 ± 2.4
35	stop $\frac{1}{2}$	-5.3 ± 0.7	11.7 ± 1.2
36	stop $\frac{3}{4}$ A	-4.4 ± 0.6	10.7 ± 1.0
37	hi rate	-3.6 ± 1.0	14.1 ± 1.6
38	aperture	-4.0 ± 0.9	12.9 ± 1.5
39	stop $\frac{3}{4}$ B	-4.1 ± 0.8	9.1 ± 1.3
Average		-4.2 ± 0.3	10.9 ± 0.6

Table 7.4: Table of simulation to data ρ and δ fit results in units of $\times 10^{-3}$. These values of ρ and δ are from the same fits for $P_{\mu\xi}$ reported in the previous section.

Bibliography

- [1] H. Yukawa. *Proc. Phys-Math. Soc. Japan* **17**, 47. 1935.
- [2] S. Neddermeyer and C. D. Anderson. *Phys. Rev.***51**, 884. 1937.
- [3] S.Tomonaga and G.Araki. *Phys. Rev.***58**, 314. 1940.
- [4] M.Conversi, M.Pancini and O.Piccioni. *Phys.Rev.***71**, 209. 1947.
- [5] C.Lattes, H.Muirhead, G.Occhialini and C.Powell. *Nature***159**, 694. 1947.
- [6] S.Sakata and K.Inoue. *Proc. Phys-Math. Soc. Japan* **24**, 843. 1942.
- [7] R.E. Marshak and H.A. Bethe. *Phys.Rev.* **72**, 506. 1947.
- [8] M. Goldhaber, L. Grodzins, and A. W. Sunyar. *Phys. Rev.***109**, 1015-1017. 1958.
- [9] Review of Particle Physics, *Phys. Rev. D* **66**,353, 2002.
- [10] V. Bargman, L. Michel, and V.L. Telegdi. *Phys. Rev. Lett.***2**, 435. 1959.
- [11] J. D. Jackson. *Classical Electrodynamics – 3rd ed.* John Wiley & Sons, New York, 1998.
- [12] N.L. Rodning, *TWIST* Physics Motivation, Unpublished Paper, March 14, 2002
- [13] G. Marshall, *TWIST* Motivation and Overview, Unpublished Presentation for NSERC Review, Jan. 2003.
- [14] Marshall, G. et. al. *NSERC Request Form 101, Part II.* September 2002.
- [15] Beltrami. *Pys. Lett. B* **194** (1987) 326.
- [16] Schenck. *Muon Spin Rotation Spectroscopy: Principles and Applications in Solid State Physics*, Adam Hilger Ltd., Bristol, England, 1985.
- [17] Cox, S. F. J. *Implanted Muon Studies in Condensed Matter Science*, J. Phys. C: Solid State Phys. **20** (1987) 3187-3319.
- [18] Stoker, D. P. *Search for Right Handed Currents by Means of Muon Spin Rotation.* Ph.D. Thesis, Lawrence Berkely Laboratory, University of California (1985).
- [19] Brewer, Jess. Private Communications. University of British Columbia, Fall 2002.
- [20] Raghavan, P. *At. Data Nucl. Data Tables***42** (1989) 189.

-
- [21] Cohen, E.R. *Rev. Mod. Phys.***59** (1987) 1121.
- [22] F. Halzen and A.D. Martin, *Quarks & Leptons: An Introductory Course in Modern Particle Physics* (John Wiley & Sons, Inc.,1984).
- [23] S. Eidelman *et al.*, *Phys. Lett.* **B592**, 1 (2004).
- [24] L. Michel, *Proc. Phys. Soc.* **A63**, 514 (1950).
- [25] C. Bouchiat and L. Michel, *Phys. Rev.* **106**, 170 (1957).
- [26] T. Kinoshita and A. Sirlin, *Phys. Rev.* **108**, 844 (1957).
- [27] W. Fetscher and H.-J. Gerber, *Precision measurements in muon and tau decays*, in *emphPrecision tests of the standard electroweak model* (World Scientific, 1995).
- [28] W. Fetscher, H.-J. Gerber, and K.F. Johnson, *Phys. Lett.* **B173**, 102 (1986).
- [29] P. Langacker and S.U. Sandar, *Phys. Rev.* **D40**, 1569 (1989).
- [30] M.V. Chizhov, hep-ph/0405073.
- [31] M.V. Chizhov, hep-ph/0402105.
- [32] E. Frlež *et al.*, *Phys. Rev. Lett.* **93** 181804 (2004).
- [33] Q.R. Ahmad *et al.*, *Phys. Rev. Lett.* **87**, 071301 (2001).
- [34] Q.R. Ahmad *et al.*, *Phys. Rev. Lett.* **89**, 011301 (2002).
- [35] G. Prézeau *et al.*, hep-ph/0409193.
- [36] J. Peoples, Columbia University, thesis, Nevis Report No. 147 1966 (unpublished).
- [37] B.A. Sherwood, *Phys. Rev.* **156**, 1475 (1967).
- [38] D. Fryberger, *Phys. Rev.* **166**, 1379 (1968).
- [39] S.E. Derenzo, *Phys. Rev.* **181**, 1854 (1969).
- [40] F. Liu, Texas A&M University, thesis, 1994 (unpublished).
- [41] [Los Alamos TPC experiment proposal]
- [42] H. Burkard *et al.*, *Phys. Lett.* **160B**, 343 (1985).
- [43] N. Danneburg *et al.*, *Phys. Rev. Lett.* **94**, 021802 (2005).
- [44] I. Beltrami *et al.*, *Phys. Lett.* **B194**, 326 (1987).
- [45] A. Jodidio *et al.*, *Phys. Rev.* **D34**, 1967 (1986).
- [46] B. Balke *et al.*, *Phys. Rev.* **D37**, 587 (1988).

-
- [47] R.S. Henderson *et al.*, hep-ex/0409066.
- [48] <http://midas.triumf.ca>
- [49] F. James, "Fitting tracks in wire chambers using the Chebyshev norm instead of least squares," *Nucl. Instr. Meth.* **211** (1983) 145.
- [50] G. Lutz, "Optimum track fitting in the presence of multiple scattering," *Nucl. Instrum. Meth.* **A273** (1988) 349.
- [51] R. Barlow. "Systematic Errors: facts and fictions", hep-ex/0207026 (2002).
- [52] Y. Davydov *et al.*, Nucl. Instr. and Meth. **A461**, 68 (2001).
- [53] J.R. Musser *et.al.* Phys. Rev. Lett. **94**, 101805 (2005).
- [54] A. Gaponenko *et al.* Accepted to Physical Review D, March 2005. arXiv preprint hep-ex/0410045.
- [55] C. Boucher-Véronneau. The *TWIST* Solenoid Magnetic Field. TRIUMF Summer Student Report, 2004.
- [56] R. E. Behrends, R. J. Finkelstein, and A. Sirlin. "Radiative corrections to decay processes," Phys. Rev. **101**, 866 (1956).
- [57] S. M. Berman. "Radiative corrections to muon and neutron decay," Phys. Rev. **112**, 267 (1958).
- [58] A. B. Arbuzov. "First order radiative corrections to polarized muon decay spectrum," Phys. Rev. **112**, 267 (2002).
- [59] A. Abruzov, A. Czarnecki, and A. Gaponenko, "Muon decay spectrum: Leading logarithmic approximation," Phys. Rev. **D65**, 113006 (2002) hep-ph/0202102.
- [60] A. Arbuzov and K. Melnikov, "Corrections to electron energy spectrum in muon decay," Phys. Rev. **D66**, 093003 (2002) hep-ph/0205172.
- [61] A. Arbuzov, "Higher order QED corrections to muon decay spectrum," JHEP **03**, 063 (2003), hep-ph/0206036.
- [62] A.B. Arbuzov, "Virtual and soft pair corrections to polarized muon decay spectrum," JETP Lett. **78**, 179 (2003), hep-ph/0301114.
- [63] J. Korrington, Physica XVI(1950)601.
- [64] A. Abragam, The Principles of Nuclear Magnetism, Oxford, 1961, p.355.
- [65] S.F.J. Cox, S.P. Cottrell, M. Charlton, P.A. Donnelly, S.J. Blundell, J.L. Smith, J.C. Cooley, W.L. Hulst, Physica B 289-290(2000)594.

-
- [66] R.S. Hayano, Y.J. Uemura, J. Imazato, T. Yamazaki, R. Kubo, *Phys. Rev.*, **20B**, 850 (1979).
- [67] E.W. Collings, F.T. Hedgcock, *Phys. Rev.*, 126(1962)1654.
- [68] O. Hartmann, E. Karlsson, E. Wackelgard, R. Wappling, D. Richter, R. Hempelmann, T. Niinikoski, *Phys. Rev.*, 37B(1988)4425.
- [69] W. Schilling, *Hyperfine Int.*, 4(1978)636.
- [70] D.C. Brice, *Phys. Lett.*, 66A(1978)53.